

GRAVITON INDUCED MONOJET PRODUCTION IN CMS WITHIN ADD TYPE LED

A THESIS SUBMITTED TO
THE GRADUATE SCHOOL OF NATURAL AND APPLIED SCIENCES
OF
MIDDLE EAST TECHNICAL UNIVERSITY

BY

UĞUR EMRAH SURAT

IN PARTIAL FULFILLMENT OF THE REQUIREMENTS
FOR
THE DEGREE OF MASTER OF SCIENCE
IN
PHYSICS

JUNE 2010

Approval of the thesis:

GRAVITON INDUCED MONOJET PRODUCTION IN CMS WITHIN ADD TYPE LED

submitted by **UĞUR EMRAH SURAT** in partial fulfillment of the requirements for the degree of **Master of Science in Physics Department, Middle East Technical University** by,

Prof. Dr. Canan Özgen
Dean, Graduate School of **Natural and Applied Sciences**

Prof. Dr. Sinan Bilikmen
Head of Department, **Physics**

Prof. Dr. Meltem Serin
Supervisor, **Physics Department**

Examining Committee Members:

Prof. Dr. Namık Kemal Pak
Physics Department, METU

Prof. Dr. Meltem Serin
Physics Department, METU

Prof. Dr. Mehmet Zeyrek
Physics Department, METU

Prof. Dr. Sibel Başkal
Physics Department, METU

Prof. Dr. Albert De Roeck
Physics Department, University of Antwerp

Date:

I hereby declare that I have obtained and presented all information in this document in accordance with academic rules and ethical conduct. I also declare that, as required by these rules and conduct, I have fully cited and referenced all material and results that are not original to this work.

Name, Last Name: UĞUR EMRAH SURAT

Signature :

ABSTRACT

GRAVITON INDUCED MONOJET PRODUCTION IN CMS WITHIN ADD TYPE LED

Surat, Uğur Emrah

M.Sc, Department of Physics

Supervisor : Prof. Dr. Meltem Serin

June 2010, 88 pages

The discovery reach for the ADD-type Large Extra Dimension (LED) scenario in the CMS Experiment at the LHC is presented by looking at the Monojet + Missing Energy signature, which arises as a result of a single graviton emission accompanied by a quark or gluon. Using Monte Carlo generated events, two LHC run scenarios were considered and compared namely a center-of-mass energy of 14 TeV and integrated luminosity of 100 pb^{-1} , and a center-of-mass energy of 10 TeV and integrated luminosity of 200 pb^{-1} . Details from extensive trigger studies are presented and offline selection techniques that optimize the signal excess over backgrounds are highlighted. As a result of this study, it is shown that the existing Tevatron limits on the ADD model can be improved through the implementation of this analysis in CMS Experiment with a factor of 3 using the the early LHC data.

Keywords: Beyond Standard Model, Large Extra Dimensions, ADD, CMS, Jet-Missing Energy

ÖZ

ADD TİPİNDEKİ GENİŞ EKSTRA BOYUTLARDA GRAVİTON YOLUYLA OLUŞTURULAN TEKİL JET KANALININ CMS’TE ÜRETİLMESİ

Surat, Uğur Emrah

Yüksek Lisans, Fizik Bölümü

Tez Yöneticisi : Prof. Dr. Meltem Serin

Haziran 2010, 88 sayfa

Bu çalışmada, Kayıp İzdüşüm Enerjisi + Tekil Jet kanalında simüle edilen Geniş Ekstra Boyutlar, ADD modelinin öngördüğü çerçeve içerisinde sunulmuş ve CMS dedektöründe bir kuark yada gluon tarafından tetiklenen bu graviton salınımına ilişkin keşif limitleri belirlenmiştir. İki ayrı LHC senaryosu, kütle merkezi enerjisi 10 TeV ve 14 TeV olan proton demetleri için sırasıyla 100 pb^{-1} ve 200 pb^{-1} entegre ışınım enerjisinde Monte Carlo üreticileri tarafından üretilmiş ve karşılaştırmalı olarak ele alınmıştır. Analiz için öngörülen tetikleme çalışmaları detaylandırılmış ve hedeflenen yüksek enerjili hadronik oluşuma erişebilmek için uygulanan optimizasyon teknikleri karşılaştırılmıştır. Sonuç olarak, Tevatronda ADD modeli için geçerli limitlerin, LHC verileri kullanılarak, bu analiz metodları üzerinden 3 kat artırılabilceği gösterilmiştir.

Anahtar Kelimeler: Standard Model ve Ötesi, Geniş Ekstra Boyutlar, ADD, CMS, Jet-Kayıp Enerji

ACKNOWLEDGMENTS

It is a great pleasure to thank those who made this thesis possible and only some of whom, it is possible to give particular mention here.

This thesis would not have been possible without the help, guidance and patience of my supervisor, Prof. Dr. Meltem Serin. She never gave up believing in me and without her encouragement and unwavering support, there was no way to finish this dissertation.

I am grateful to Albert De Roeck for involving me in Exotica group at CMS and tending my interest during my stay at CERN. He taught me how to work hard and play hard to approach a research problem. There is much to learn from his dedication and wealth to science.

I would like to thank all other monojetters, starting from Leonardo Sala who was most responsible for this challenging research. Thanks to Leonardo Benucci devoted most of his precious time to the MonoJet study and taught me how to write academic papers in the first place.

A special thanks goes to my colleague, Marco Cardaci who was always there to meet and talk about my ideas with his insightful remarks. Our joyful work and discussions stimulated me throughout this study.

Thanks to all the people in METU HEP group for their participation in my studies and further thanks to our current project leader Mehmet Zeyrek for his counseling and unconditional support.

I greatly thank Namık Kemal Pak for his valuable remarks and guidance in writing the theoretical part of the manuscript. In his wisdom, I got considerable amount of comfort during the final stages of this work. I also thank Sibel Başkal for her significant comments and proof-reading of this thesis.

I am greatly indebted to Halil Gamsızkan (Aga) who has introduced me all the fundamental stuff I was struggling to understand in the first place not to mention his unparalleled understanding on programming. He has been a friend as well as a mentor and I learned much from his Flying Spaghetti Monster.

Very thanks to Sezen Sekmen (Mihtar Sivridil) for her crucial touches extremely valuable for me on both an academic and personal level. She proofread and marked up this thesis and pushed me to think over how a person lives only with vegetables.

Thanks to Efe Yazgan for his intriguing discussions on many things with a kind of melancholy and Yasemin Uzunefe Yazgan for her cheerful friendship. I also would like to thank to the members of our music band at CERN, Bilge Demirköz, Yetkin Yılmaz and Sinan Kудay for the delightful moments we had together. I owe thanks to Selçuk Bilmiş, Aydın Ayhan, Iliana Vasileva Akin and all the folks at CERN for their company and being fun to be with.

I finally give thanks to my family who raised me to become the person I am today.

...

This thesis should have been carrying the deficiency of focusing on one particular problem but it is not an obstacle to iterate what is already known. For any errors or inadequacies may remain in this work, the responsibility is belong to me.

CERN visits during the work included in this thesis were financially supported by The Turkish Atomic Energy Authority (TAEK) CERN Project. Special thanks to Nergis Telyakar for her kind interest and prompt responses.

TABLE OF CONTENTS

ABSTRACT		iv
ÖZ		v
ACKNOWLEDGMENTS		vi
TABLE OF CONTENTS		viii
LIST OF TABLES		xi
LIST OF FIGURES		xiii
 CHAPTERS		
1	INTRODUCTION	1
1.1	A Picture of Matter and Fundamental Forces	2
1.1.1	The Physical World and The Mind	2
1.1.2	Fundamental Forces	4
1.1.3	Spacetime and Dimensionality	5
1.2	Development of Extra Dimensions and Unification of Fundamental Forces	7
1.2.1	Early Attempts	7
1.2.2	Gauge Era and the Reflections on Spatial Manifolds	8
1.2.3	Hierarchy Problem and the Further Progress	9
1.2.4	ADD via LED	10
1.3	A Preamble for the Analysis	11
1.3.1	Identification of the Observables in Extra Dimensions	11
1.3.2	Out of Nothing into Something New : ME_T	12
1.3.3	Occam’s Razor and The MonoJet Signature	12
1.3.4	Inverse Mapping of the Data	13

2	COMPACTIFICATION VIA LARGE EXTRA DIMENSIONS WITHIN ADD MODEL	15
2.1	Kaluza Klein Theory	15
2.2	Analogy with the ADD Model	18
2.3	Braneworld Theories	20
2.4	Reconciling Compactification on Braneworld: ADD Scenario	22
2.4.1	Constraints on the Parameter Space	24
3	LHC AS A NEW FRONTIER OF PHYSICS	25
3.1	Overview to Large Hadron Collider	25
3.2	Luminosity Challenges	25
3.3	CMS(Compact Muon Solenoid) Detector	29
3.3.1	Interaction of Particles with Material	30
3.4	The Tracker	31
3.5	ECAL	32
3.6	HCAL	34
3.6.1	HCAL Partitions	35
3.7	The Muon System	36
4	CMS TRIGGER SYSTEM	38
4.1	Introduction	38
4.2	Requirements of the Trigger System	39
4.2.1	Physics Requirements	39
4.2.2	System Requirements	40
4.2.3	Rate Requirements	40
4.2.4	Structural Requirements	40
4.3	L1 Trigger System	41
4.3.1	L1 Calorimeter Trigger	42
4.4	High Level Trigger(HLT)	44
5	CMSSW : PHYSICS ANALYSIS IN CMS EXPERIMENT SOFTWARE ENVIRONMENT	45
5.1	Reconstruction	45
5.1.1	Reconstruction of Objects	45

5.1.2	Reconstruction of Events	46
5.2	CMS Experiment Software	48
5.2.1	Event Data Tiers	48
5.2.2	PAT:Physics Analysis Toolkit	49
5.2.3	CSA07 Production	51
6	ANALYSIS	52
6.1	Introduction	52
6.2	Direct Graviton Production Mechanism	52
6.3	Current Limits	53
6.4	Monte Carlo Generation of Signal and Background Samples and Re- construction	54
6.4.1	Signal Generation	57
6.4.2	Background Generation	59
6.5	Trigger Selections	60
6.5.1	Trigger Selection and Optimization for 14 TeV Analysis	60
6.5.2	Implementation of H_T and MH_T quantities	61
6.5.3	Trigger Selection for 10 TeV Analysis	64
6.6	Signal and Background Analysis and Selections	67
6.6.1	I. Requirements at the Preselection Level	68
6.6.2	II. Charged Leptons Cleaning Cuts	69
6.6.3	III. Kinematic Cuts and QCD Reduction	69
6.6.4	IV. Imposed Topological Constraints	70
6.7	Results and Systematics	72
6.7.1	Theoretical Uncertainties	74
6.7.2	Experimental Uncertainties	75
6.8	Discovery Potential and Exclusion Limits	75
7	CONCLUSIONS	79
	REFERENCES	80
	APPENDICES	
A	ADAPTED TRIGGERS FOR 10 TeV SEARCH	85

LIST OF TABLES

TABLES

Table 2.1	Number of Extra Dimensions vs. Compactification Radius	24
Table 3.1	Important parameters at LHC	27
Table 3.2	Parameters of the CMS Superconducting Solenoid	30
Table 6.1	For the $\gamma + ME_T$ and Jet + ME_T signatures with 95% Confidence Limits specified by different experiments in TeV order	54
Table 6.2	For the Jet + ME_T signatures with 95% Confidence Limits expected at LHC in TeV order	54
Table 6.3	ADD cross sections (and errors from generation stage) as evaluated by the SHERPA program for $\sqrt{s} = 14$ TeV where all values are in terms of pb.	57
Table 6.4	ADD cross sections (and errors from generation stage) as evaluated by the SHERPA program for $\sqrt{s} = 10$ TeV for all values in terms of pb.	58
Table 6.5	Overview of the Background Statistics produced in the CSA07 for 14 TeV Analysis where (*) stands for the k-factor	59
Table 6.6	Overview of the Background Statistics for 10 TeV Analysis	59
Table 6.7	Summary of the cuts applied by $H_T + MH_T$ Trigger	64
Table 6.8	Possible Trigger paths concerned for ADD Monojet at 10 TeV Study	66
Table 6.9	Selected events of each group of cuts for the background samples of 14 TeV case normalized to 100 pb^{-1}	71
Table 6.10	Number of selected events for each group of cuts in four 14 TeV signal sub- samples, normalized to 100 pb^{-1} . Uncertainties on efficiencies are only statistical.	71
Table 6.11	Number of selected events for each group of cuts in the 10 TeV background samples normalized to 200 pb^{-1}	72

Table 6.12 Number of selected events for each group of cuts in four 10 TeV signal subsamples, normalized to 200 pb^{-1} . The final efficiencies are quoted with only statistical uncertainties	72
Table 6.13 Overview of the Systematical Uncertainties given for 14 TeV and 10 TeV CM cases	75
Table 6.14 Survived Background Events after combining all results	76
Table A.1 Efficiency of the triggers before the selections are applied together with the number of events survived	86
Table A.2 Efficiency of the triggers after the selections are applied together with the number of events survived	87

LIST OF FIGURES

FIGURES

Figure 2.1 (a) KK Picture with gravity access to the whole space time, characterized by the spatial dimensions of R , where SM particles are confined on a subspace (internal manifold) whose compactification yields $L \ll R$. (b) Circles at each point in M^4 space.	17
Figure 2.2 KK configuration of M^4 space, where nonzero modes propagate inside the cylinder	18
Figure 2.3 The solution interpolates between $\phi = V$ and $\phi = -V$ as extra coordinate z runs from $-\infty$ to $+\infty$	21
Figure 2.4 The solid line represents our <i>Braneworld</i> where only gravity can live on the bulk	23
Figure 3.1 LHC Complex	26
Figure 3.2 CMS Overview	29
Figure 3.3 CMS tracker layout	31
Figure 3.4 Transverse section through the ECAL, showing geometrical configuration.	33
Figure 3.5 Layout of HCAL Barrel and Endcap detectors. Inner phi segment of a wedge.	35
Figure 3.6 HCAL Partitioning	36
Figure 3.7 Side view of MB and ME Muon systems	37
Figure 4.1 Overview of the Level 1 Trigger	43
Figure 5.1 PAT Workflow	50
Figure 6.1 Different production modes for the Direct Graviton channel within ADD Framework	53

Figure 6.2	The p_T of generated graviton (left) and the azimuthal angular difference between the leading jet and the missing transverse energy (right) at generator level, for various benchmark points. No significant discrepancies between the different ADD signals have been found.	58
Figure 6.3	Correspondence of (H_T, E_T) pair to (MH_T, ME_T) without applying any cut on a Low mass QCD Sample	62
Figure 6.4	Jet trigger algorithm	62
Figure 6.5	QCD Rate with the projection of Jet p_T^0 threshold for H_T+MH_T Trigger	63
Figure 6.6	H_T+MH_T Trigger efficiency for $M_D=2, \delta=2$ benchmark point as a function of p_T^0 threshold for different selections.	64
Figure 6.7	After $H_T > 200$ GeV, $p_T > 10$ GeV cut is applied, HLT efficiency as a function of MH_T threshold is given for different benchmark points of ADD Signal	65
Figure 6.8	On the left, the efficiencies before H_T cut is used and on the right efficiencies of different benchmark points of ADD signal after $MH_T > 100$ cut applied.	65
Figure 6.9	Comparison for the Efficiencies of the H_T+MH_T Trigger and Single-Jet trigger corresponding to the ADD signal with $M_D=2$ TeV and $\delta=2$ projected on MH_T	67
Figure 6.10	Number of jets for signal and relevant backgrounds, for $ME_T > 400$ GeV and jets with transverse momenta larger than 40 GeV at $ \eta < 3$ for 14 TeV case. A veto against three or more Jet events turns out to be the optimal cut for minimizing the QCD contribution at 10 TeV analysis requiring $MH_T > 250$ GeV with $p_T > 50$ GeV selections. Histograms are overlaid and normalized to the same area.	68
Figure 6.11	E_T and p_T distribution of the leading jet of ADD signal ($M_D = 2$ TeV, $\delta = 2$) and relevant backgrounds. Event number is normalized to 100 pb^{-1} and to 200 pb^{-1} respectively.	70
Figure 6.12	a) Angle in the transverse plane between the ME_T and the secondary jet. Selecting the events with $\phi(\text{jet } 2, ME_T) > 0.5$ may exclude a large part of the QCD together with the $t\bar{t}$ and W + Jets Backgrounds. b) The rejection is largely enhanced by requiring $\phi(\text{jet } 2, MH_T) > 0.5$ at 10 TeV case in which a further reduction would be obtained by considering the multijet contribution of two orders of magnitude.	71

Figure 6.13 ME_T and MH_T distributions after all selections applied for $\sqrt{s}=14$ TeV and $\sqrt{s}=10$ TeV respectively	73
Figure 6.14 On the right, 3 Dimensional view of a very clean monojet event simulated for the CMS Detector is seen. On the left the projection of this event on the transverse plane is given.	73
Figure 6.15 Definitions of parameters for the S_{PL} Significance Estimator	76
Figure 6.16 Discovery potential of the Monojet Signature as a function of M_D and δ for $\sqrt{s}=14$ TeV and $\sqrt{s}=10$ TeV respectively. The horizontal thick lines correspond to 3σ and 5σ significance levels.	77
Figure 6.17 The fundamental scale M_D is correlated with the minimum integrated lu- minosity of $100 pb^{-1}$ and $200 pb^{-1}$ respectively at the %95 confidence level de- termining the exclusion limit of the monojet channel.	77

CHAPTER 1

INTRODUCTION

From a philosophical point of view, one would divide our reality into two parts. The one we perceive through our senses and the other which is constructed to encounter known paradigms and phenomena through a mathematical framework. The more intersection we get, the more we understand about the universe we live in. Thus the modern science undoubtedly accepts any correlation by simply holding the rational conclusions of proposed contingent scenarios and develop new technologies like the one recently initialized at Geneva - The Large Hadron Collider (LHC).

Currently, Standard Model (SM) of Particle Physics explains the paradigm of three generations of quarks and leptons interacting with the four fundamental forces verified with a stupendous precision. Nevertheless the model itself requires a plethora of parameters like masses, interaction strengths, etc., which should be probed as an input in this framework. As a result there are theoretical speculations constraining these parameters further and explaining them in terms of more fundamental concepts, while addressing some of the unanswered problems in the context of SM, such as strong CP problem, masses of fermions, or the Hierarchy Problem, which will be mentioned later on. At LHC, the aim is to seek possible extensions to SM in the new range of energies at TeV scale or verify SM further.

In turn, before getting a physics data at LHC, there have been developed particle simulator programs able to mimic all aspects of high energy collisions, not only with regards to SM but also in wide variety of these fundamental theories. This simulations may help to physicists to refine the theories and narrow the relevant parameter space in question.

In the present study, using the tools and softwares developed at CERN for CMS (Compact Muon Solenoid) Experiment, the aim was to make a preliminary study, devoted to the direct detection of graviton stemming from ADD (Arkani Hamed - Dimopoulos - Dvali) Extra Dimensions, which would give rise to the monojet signature in CMS detector before the

startup conditions aimed at 10 TeV and later on at 14 TeV.

In order to get a deeper understanding on the development of Extra Dimensions from Riemann to our age, it would be appropriate to start by outlining some fundamental concepts in parallel to its philosophical roots for the outsiders of the field. After then, there will be a pedagogical review on the process to underline the motivation of Large Extra Dimensions (LED) then the phenomenological model that we have studied is explained in Chapter 2. In Chapter 3, design features of LHC (Large Hadron Collider) and capabilities of CMS (Compact Muon Solenoid) Experiment will be discussed respectively. Then in Chapter 4, the trigger system of CMS will be summarized followed by an introduction to the physics analysis procedures and tools for CMS Experiment in Chapter 5. The analysis performed in regard to a single jet channel of ADD Model will be presented in Chapter 6 and the improvements in the current limits of the model will be concluded in the last part for 14 TeV in comparison to 10 TeV center of mass energies at LHC.

This analysis is performed in Exotica - Monojet group in CMS Experiment at LHC and the visits to CERN during the work were financially supported by the Turkish Atomic Energy Authority (TAEK) CERN Project.

1.1 A Picture of Matter and Fundamental Forces

1.1.1 The Physical World and The Mind

It was Democritus who brought forward the idea that every kind of object was made of nondivisible particles, so called atoms (460-370 B.C), living in the void, an infinite space. Aristotle criticized Democritus for the introduction of smallest conceivable size for entities and go along with the 4 element theory (water, fire, earth and air) considering the transformations of one form into another. For Epicurus the universe was finite and eternal. Everything within, including human mind was constantly interacting via atoms.

Following the subjectivity of matter, It was also possible to propose an articulation of an object that corresponds to a structural dimensionality where one can refer a physical world, basis of the mind. However the inexplicable fashion of this view was ruled out by Descartes' Dualism. In his view, substance dualism was contrasted with all forms of materialism since recurring patterns of experience can be named as physical systems so the mind does not necessarily interconnected to this set of systems we observe through our senses. Thus the physical world reflects to the mind and the mind responds to it with some incapacibilities.

Currently, Classical Mechanics uses a continuum background of space within which classical particles, we observe directly, have 3 main characteristics, mass(energy), momentum and position. As electromagnetism developed, *charge* and *spin* are also added to those characteristics. The time rate of change is related to the change in position of particles by producing a path in which any system is forced to minimize it giving rise to the *principle of least action* put forward by Maupertuis in 1747. Then every physical characteristic is associated to a point in spacetime to construct a physical quantity so called *field*.

Regarding the intrinsic nature of the matter, the notion of action seems to be a vacuous conception from a philosophical point of view, since it does not tell us the ultimate nature of the physical world. Alternatively, there has been considered a ‘minimum visibile’, a perceptible atom in the body’s structure, which consists of a system of worlds or the inner cataclysms accounted to an atom’s behaviour. Besides being unconvincing in themselves, simultaneous negations of these arguments were jointly inconsistent with the idea that the observable world must be *casually closed*.

From Democritus to our age, the regarded picture of atoms is replaced by a reductionist way of thinking in order to explain variety of particles observed in experiments with different characteristics. In High Energy Physics, some common characteristics of particles can still be expressed in analogy with the classical physics but the new knowledge coming from their quantum nature have to be denoted with the *quantum numbers* capturing the conservation laws in particle interactions.

Thus the pragmatist methodology of Particle Physics started from discrete quantities or numbers. The exact form is given by Planck by the incorporation of quantum action h into the mathematics of quantum theory. Regarding the behaviour of matter, it is evident that there is an immediate clash between the discreteness phenomenon in quantum paradigm and the continuity approach of classical mechanics. Nevertheless, Modern Particle Physics is done within formal languages with the Quantum Theory providing the model. Often, it is not even known what the terms used in the model mean outside the proposed parameter space. The interactions between particles built on *syntactical rules* specifies the very essence of the behaviour of the particles. The physical world picture is represented by a dual reflection of matter and field, between which there is a reciprocal action giving rise to the fundamental interactions. In parallel to the Descartes’ view, it is curious if there would be so called coherent ‘brane states’ compensating the vacuum states of quantum fields as proposed by Ricciardi and Umezawa [1].

1.1.2 Fundamental Forces

Particles interact with different unique characteristics with respect to the scale we are investigating them. Among the four fundamental forces in Physics, Quantum Mechanics accounts for 3 of them, namely electromagnetic force, strong nuclear force and weak nuclear force; but not gravity. The interaction strength of strong and weak nuclear forces are dominant inside the atomic nucleus but they are confined over a limited range. Over tiny distances at the sub nuclear level $\sim 10^{-18}$ m, they are stronger than either electromagnetic force or gravity. In this formalism, gravity is the weakest force observed so far and fades over small distances but it has an infinite range as electromagnetism separating it from nuclear forces. All except gravity can be understood through SM and the implementation of gravity to the SM appears as a blindspot in the current state. General Relativity is a theory concerning Gravity, however when applied to the quantum theory, it suggests inconsistent results with experiments such as infinite energies. It should be also noted that, there is a recent approach discussing the entropic origin of gravity with many degrees of freedom as suggested by Erik Peter Verlinde [2]. In this approach, when a stimulation of a statistical tendency increases the entropy of system, it can be assembled by Gravity.

These four forces are considered as fundamental, meaning that any other force that would be encountered is expected to behave as one of these or a combination of them. The strong force balances out the electromagnetic repulsion, and without its contribution, complex structures could not exist in any known form meaning that there wouldn't be such a thing as atomic nucleus.

Essentially, the interactions with fundamental forces is achieved by natural force carriers coming with intrinsic properties given by spin quantum numbers. These force carriers are called bosons where the word 'boson' comes from the bose statistics of the particles having integer spins just like the fermions obeying fermi statistics of the spin half particles.

The pedagogical process which forces Physicists to invent such a mechanism was initiated with the invention of Gauge Symmetry by Hermann Weyl in 1918 [3]. Following that, spin 1 particles such as photons, carriers of the electromagnetic force, travel with the speed of light with no mass, as opposed to the particles which conveys the weak force, W^+ , W^- and Z^0 , are considered to be massive. Gluons are the massless strong nuclear force carriers having eight distinct forms mediating color charge interactions of quarks in Quantum Chromodynamics (QCD). Since colour charge is conserved inside hadrons, the gluons should carry at

least 2 colour charges as they interact also by themselves.

It is equally likely that one might propose a hypothetical particle as a mediator of Gravitational Interactions named as Graviton. This particle is characterized as a spin 2 particle and a possible detection of such a particle using ADD Mechanism at LHC is the subject of this study.

1.1.3 Spacetime and Dimensionality

The set of properties of matter occupies a physical spacetime that can be defined as a boundless extend in which particles are distributed through, on top of its time component.

Ever since Euclid ‘The father of Geometry’ described the axioms of a flat space, there were intense debates about its reflection to the physical world like Kantian interpretation reconciling Newton and Leibniz views. Finally this guiding ideas were encapsulated by Riemann with the invention of non-euclidean geometry accepting all the axioms of Euclid except the postulate of parallels.

The transition from Euclidean geometry to that of a Riemann replaced also the action at a distance principle with the one based on an infinitely near action by regarding the uniformity of action in nature. Thus, it can be concluded that Euclidean Finite Geometry is replaced by Riemann’s Infinite Geometry in 18th century. Eventually, the progress in infinite geometry by regarding the intrinsic properties of the objects (topology and differential geometry) made it possible to replace the concept of space by manifolds understood in terms of contemporary considerations of geometrical features. Today, Modern Geometry has common mutual bounds with Physics referring to the Theory of Relativity or String Theory.

The journey from the notion of geometry through the concept of dimension was surely pioneered by Pythagoras of Samos(c. 569-475 BC) with his famous pythagorean theorem but it was Aristotle who developed the concept of dimension in his work *De Caelo et Mundo* (On the Heavens) by considering the division of a magnitude in 3 directions as a triad.

With the definition of space in mind, dimension can be thought as a notion of specifying independent directions for a given space while no rigorous definition exists from a mathematical point of view. The mutual orthogonality is proposed by Rene Descartes by defining the cartesian coordinates in the 17th century. Then the geometric figures, could now be represented analytically, i.e., with functions and equations.

Evidently, the synthese that casts light on this formalism was developed by Leibniz who first argued that space and time has a mutual relationship having no independent existence.

In general, time is considered to be a temporal dimension responsible for a measurement of a physical change.

Describing the world as spatially 3 dimensional is actually related to a very strong symmetry. Klein four-group or *Vierergruppe* is a quadratic group $Z_2 \times Z_2$ behave as a fundamental group of S since three elements of order 2 are interchangeable in this notation.

If the fundamental interactions of particles built up the space (or the other way around), there should be a unitary symmetry argument associated to the every fundamental force we mentioned. Then the gauge group $U(1)$ for the unit circle in a complex plane can be considered as an arbitrary angle in 3 dimensional space which corresponds to the Electromagnetic force (QED). Considering the very small mass difference between the proton and neutron, a particle can be thought to have a 2 folded dimensionality captured by the group $SU(2)$ referring the weak interaction. The unification of these forces requires the multiplication of the symmetries, so that in Electroweak Symmetry, one can consider $U(1) \times SU(2)$ symmetry argument. The next step is to construct $SU(3)$ symmetry having 3 elements of quark combinations known as QCD. Eventually the SM of Particle Physics describes the unification of 3 fundamental forces by assigning $U(1) \times SU(2) \times SU(3)$ symmetry not surprisingly. Moreover, the $SU(N)$ system can be speculated to have a predictive power in explaining the patterns of particles, which haven't been observed yet. The $SU(N)$ group has a dimension of $N^2 - 1$, thus in above pattern, we can see the consistency with the number of gauge bosons corresponding to the each group as stated in the previous subsection. Therefore we end up with 1 gauge boson for EM, 3 for Weak Nuclear force and 8 gluons for Strong Nuclear force as dimensionality dictates.

The quarks demonstrate why the $SU(3)$ symmetry is held but a further inspection with experimental data can bring forward an explanation for *Symmetry Breaking* mechanism since the mass of quarks varies dramatically. Adding gravity to this picture is a bit more challenging but one can use the feature of isomorphism in the category of smooth manifolds to complete the picture. So there can be considered an invertible function, which maps one differentiable manifold to another, such that both the function and its inverse remains smooth. Therefore $Diff(M)$ symmetry can be accounted for Gravitational Interactions.

1.2 Development of Extra Dimensions and Unification of Fundamental Forces

1.2.1 Early Attempts

Die lineale Ausdehnungslehre (The Theory of Linear Extension, 1844) by Hermann Grassmann was the first book which proposed a system whereby space and geometric components and descriptions could be extrapolated to the other dimensions. However this book consisted of more philosophy than mathematics and it was described even by Klein as almost unreadable.

Thus, the credit for the discovery of the platonic solids in 4 dimensional space is accepted to go to Ludwig Schläfli with his book *Theorie der vielfachen Kontinuität* (Theory of Continuous Manifolds, 1852) with an intensely analytic approach, which went far beyond what had been done before. Another accepted formalism which describes geometry of arbitrary dimensional manifolds is dating back to the study of Bernhard Riemann in 1854 with his lecture on curved geometry of n dimensions.

Three decades after, inspired by these studies, an English Theologian, Edwin Abbott tried to visualize how an entity confined on a brane (2D) perceives the world of 3 dimensions in his famous book *Flatland: A Romance of Many Dimensions* in 1884. Having this new concept, the amplified sensations through spatial objects has begun to be realized and the first speculations in Physics was started to be made.

Trained at Oxford as a Physicist as well as a Mathematician, Charles Howard Hinton, who introduced the geometry of 4-cube called tesseract was first to speculate fourth dimension could explain some problems in physics and finally in *Scientific Romances*, he tackled the all-important ether that resides in the fourth dimension.

In the beginning of 19th century, the novel *The Time Machine* by H.G.Wells was one of the forerunners of science fiction genre but actually the true interpretation of fourth dimension was manifested in this book. Rather than the fiction, the science hidden inside was reflected by the Einstein's Special Theory of Relativity in 1905. The democratic behaviour of gravity inspired Einstein for his revolutionary idea in which gravity is not a force but the feature of spacetime itself. Thus, it was the primordial work, where the ultimate velocity in our universe was put in question and the mass manifested itself as an another form of the energy.

4 years later, Hermann Minkowski responded to this outstanding idea in which space and time are not separated entities but they are intertwined through a 4 dimensional manifold in parallel to the Leibniz's view. As a striking result, all Maxwell's equations could be written

in a very simple form.

In 1914, the first extra dimension theory aimed to unify gravity and electromagnetism was published by Gunnar Nordstrom by adding a new spatial dimension to his metric theory of gravitation. The role of the electromagnetic potential was mimiced by a scalar gravitational field [4]. However, the theory lacked of relativistic corrections that Einstein was about the publish in 1915 [5]. In General Relativity, as well as in Special Relativity, the universe was 4 dimensional and the extra-dimension considered by Einstein was time-like.

1.2.2 Gauge Era and the Reflections on Spatial Manifolds

‘ We must never lose sight of the inseperable theoretical whole when we enquire whether these sciences interpret rational reality which proclaims itself in all subjective experiences of consciousness, and which itself transcends consciousness: that is the truth forms a system.’

Hermann Weyl–Space Time Matter

After Einstein’s Gravitational Theory was established, there were number of attempts to generalize it and the first proposal was given by Hermann Weyl in 1918, where his theory contained only a vector field that corresponds to the EM (Electro Magnetic) interactions in addition to the gravitational field. In the Geometry of Weyl, length was path dependent so that two bodies congruent at one spacetime point need not be congruent at another if they followed different world lines.

Einstein objected that this path dependence in Weyl’s spacetime geometry left it without determinate empirical content, since in a Weyl space, the geometrical concept of the spacetime interval could, therefore, not be given a univocal empirical interpretation.

Although this theory was a failure, the strongest argument for the theory was the introduction of Gauge Invariance corresponding to the conservation of the electric charge in the same way the coordinate-invariance corresponding to the conservation of energy and momentum. Thus, this work had a critical importance for the development of the Gauge Theory because of the introduction of non-metrical geometry to the Physicists. Hence the study has leaded the subsequent works in the field and has become a steering mechanism.

After the deep impact of Weyl’s paper, a pure classical attempt was done by Kaluza in his 1922 paper, within the context of 5D manifold where the meaning of 5th coordinate, ‘ x_0 ’ would be interpreted as a ‘curling up’ of the 5 dimensional space in one direction and the fields constructed in this framework did not depend on this extra coordinate. To conceptualize the relationships between Kaluza’s ideas and the quantum problems of De Broglie and

Schrodinger at that time, Oscar Klein assigned a circular topology to this extra coordinate (usually taken in plack length) which cannot be perceived in macroscopic scales. So the *Compactification Problem* has been coined which works also at quantum level given by the Kaluza Klein (KK) Theory. In this model, $U(1)$ local gauge invariance of electromagnetism comes about because of the circular geometry of extra dimension and the relativity was invariant under the rotations around this circle. The fields living in a 5 manifold is naturally expanded by fourier series in this extra coordinate corresponding to the characteristic energy modes inversely proportional to the radius of the compact dimension. Supposing two tiny circles at each point in spacetime, the symmetry group would be $U(1) \times U(1)$, thus an observer in our 4 dimensional world would observe 2 different types of photon. This idea can be further be speculated such that, at each point, there is a compact space or a manifold with many dimensions would have unify gravity with all the other forces. The details of the KK theory can be found in Chapter 2 of this thesis.

1.2.3 Hierarchy Problem and the Further Progress

The route opened by the invention of the Gauge Theory has led to the discovery of weak interaction via observation of W and Z Gauge bosons in prior to the 1970's by the confirmation of Electroweak Theory (EW). This Theory is originated from weak isospin symmetry embodied in the quark and lepton doublets together with weak hypercharge phase symmetry where neutrinos are massless. Precise measurements over the past years has proved that the EW theory as a Quantum Field Theory, at the 246 GeV energy scale.

This whole approach is based on Quantum Field Theory (QFT) which considers matter as a form of point-like object and works remarkably on the description of quarks and leptons. However, when a graviton is involved in the process, during the adjustments on the SM parameters, closed loops containing virtual particles cause divergences which resulted with infinite number of answers. The most important divergences are called Ultraviolet (UV) ones stems from short scale distance and time scale incosistencies.

In early 1960's, another approach had started to be developed to handle the ambiguities described above. The familiar point-like bosons in QFT are replaced by 1 dimensional strings and the different vibration modes of these strings are considered for the observed characteristics of particles like flavor, mass, charge and spin. Then the action of string theory minimized the area swept by this string and turn out to be simplified since no arbitrary interaction terms are required in this formalism.

String theories also have a prediction of several extra, unobservable, dimensions to the universe thus, the unifying group for the dimensionality of spacetime is taken either for $SO(32)$ or $E(8) \times E(8)$ symmetry. Using this approach, it is also possible to estimate the string tension from the graviton mode, which corresponds to 10^{39} tons. Such a tremendous tension would result with the contraction of string to the Planck length 10^{-35} meters and cause the construction of a closed string, which is symbolically represented as Graviton. Moreover, the fundamental mode of vibration of the string give rise to a particle with a mass of the order of the planck scale ($10^{19} GeV \sim 10^{-4} gram$).

Nevertheless, the obvious disparity between the orders of the magnitudes of the planck scale ($10^{19} GeV$) and the EW Scale ($246 GeV$) remains unanswered in the context of SM and known as the Hierarchy Problem[6]. Since the parameters of the SM are adjusted so that the theory fits the observed electroweak scale, the argument essentially involves the Higgs mechanism, which is responsible for the conversion of energy into the mass in any process of the SM. This feature raises a significant yet unknown limitations on the planck mass, comparable to the scale at which new physics would appear. Hence, this is a crucial attribute that can be used as a guideline for new physics as the significant number of unresolved problems in SM can only be untangled by the experimental data. It is our hope however that the challenges ahead at LHC will pave the way.

1.2.4 ADD via LED

Currently, the tendency of the models discussing the dimensionality of $(3+N) + 1$ our space time shifted towards the Brane World or a Domain Wall Theory in which ordinary light particles are confined in a potential well, narrow along N spatial directions and smooth along others. Eventually if there are free particles living outside this brane, the collisions of this particles with the brane may end up with an high energy release, that can be seen by the observer confined on the brane.

In the Brane World context, the space-time manifold is considered to be $M^{3,1} \times S$ where M is the Minkowski space with 1 time dimension and S is a compact manifold. Neglecting the brane tension and without resorting the symmetry argument, one way to solve the hierarchy problem is to use geometry instead as proposed in ADD model. Then if there are sufficient dimensions of large size, it is possible to bring the Planck scale all the way down to the EW scale. So one can redefine the power law in short distances for an observer outside our domain wall(brane). Thus, for the case of n extra spatial dimensions, all curled up with a

radius of R , the power law yields $1/r^{n+2}$ at the compactification scale. Thus using different compactification mechanisms in analogy with the string theory at this short distance scale, one can introduce extra spatial dimensions denoted by δ implemented to our brane.

In this context, Large Extra Dimension (LED) theory refers to the class of models which incorporate compactified dimensions to our brane by replacing the M_{pl} with so called an effective scale (M_D) would be in the reach of LHC. The size of extra dimensions are ‘large’ compared to the planck scale entitles this type of extra dimensions. Using LED, the hierarchy problem of SM can be naturally reduced from an UV one to an infrared (IR) one and there is also a possibility of having an interface with the String Theory [7].

Hence, a graviton, described as a closed string can be embedded to this compactified dimensions with certain sizes and enhance the strength of gravitational interaction at this scale. In this way the KK picture is just reintroduced by replacing the circular topology with compact toroidal geometry and such a mechanism immediately removes the hierarchy problem by modifying the newtonian potential at M_D scale. The details of the Braneworld theory and ADD model is discussed in the next chapter extensively. Randall Sundrum (RS) model is an alternative scenario for the compactification mechanism[8].

1.3 A Preamble for the Analysis

At this stage, we can summarize some crucial aspects about the analysis concerned in this study.

1.3.1 Identification of the Observables in Extra Dimensions

Before proceeding to the discussion of a measurement of a particle in an extra dimension, the variety of possibilities stemming from different philosophical grounds should be understood.

The main thought experiments accepted are based on Confinement and Ignorance Hypothesis. Here we will not consider them individually but for the Ignorance Hypothesis where the trajectories of higher dimensional particles measured by a lower dimensional perspective cannot be known precisely, see [66].

The case we are interested in the context of ADD Theory consists of a mixed interpretation in which some of the particles (baryonic particles) are confined to the brane we live in but a graviton as a bosonic particle can live outside of the brane.

1.3.2 Out of Nothing into Something New : ME_T

For something to be declared as invisible, we must know it exists, then knowing the existence actually is to say that it is no longer invisible paradoxially thus the term ‘missing’ is found appropriate to imply the meaning behind.

Considering high energy collisions, it is known that the rest mass of the particles is defined by the norm of its momentum. Thus the corresponding energy can be measured from the annihilation in the rest frame where graviton might actually penetrate to our brane, producing apparent violations of conservation of energy.

In this sense, the variability of an effective rest mass is seen as a covariant generalization of a flat space physics. The hidden energy stored in the extra dimensional motion can be recorded by an observer with respect to the projection on the transverse energy plane (E_T space of the detector). Missing Transverse Energy- ME_T is explained in detail at Chapter 5 and later on at Chapter 6.

1.3.3 Occam’s Razor and The MonoJet Signature

‘Entia non sunt multiplicanda praeter necessitatem’

William of Ockham

By taking into account the experimental capabilities, it is fair to say that we don’t know how gravity behaves at distances shorter than 10^{-4} cm and in distances larger than 10^{28} cm. However, within this interval, the inverse square law provides a good estimation for nonrelativistic gravitational interactions, where laws of nature would be different outside of it.

Similarly, it is certain that the EM interactions obey inverse square law down to the distances around 10^{-16} cm but it is an ambiguity if there would be an alteration in shorter distance scales.

The underlying quark-gluon interactions acting in small distance scales is understood in detectors as jets corresponding to a certain parton density. Descriptions for the parameters used for identifying the jets are given in Chapter 6.

At the LHC, gravitons can be produced recoiling against a quark or gluon jet as explained in Chapter 6. The large number of kinematically accessible states compensates the small gravitational coupling in order to encounter sizable cross sections. The resulting topology turns out to be an energetic monojet like signature back to back with ME_T vector.

However, there is no constraint for the envisioned graviton within ADD context to be observed in the Monojet + ME_T channel. Graviton in ADD framework can be detected in

many different channels but the most striking signature for the direct graviton production is surely the Monojet + ME_T channel because of its large cross section and the very simple topology. A competitive channel for the ADD discovery would be the interference in the diphoton production channel.

Another possibility, the Monophoton + ME_T signature, is hardly competitive with the Monojet + ME_T since QCD dijet processes constitute an excessive background in this channel [11].

It is also arguable that Unparticles can mimic both of the mentioned Monojet and Monophoton signatures. For the scalar unparticles, the discrimination for the single jet in E_T space is given [9].

As stated by the principle of parsimony above, the simplest scenario is chosen for this study since it is also based on the most reliable methodological grounds without rigorous aesthetical considerations.

1.3.4 Inverse Mapping of the Data

Determining the underlying physical theory of the TeV scale by using the LHC data can be referred as the inverse LHC problem. Among the tremendous range of possibilities, it is unlikely to construct a coherent strategy for going from data to a still-unknown theory. However, inferring a new physics scenario via phenomenological consequences is a reverse problem only for a theoretician. For an experimentalist it is just another problem [12].

For instance in the ADD scenario, we start with a particular model with a certain parameter space (M_D, δ) , study its phenomenological consequences, and try to observe this consequences in order to reach a signature space. But for a theoretician who try to reconstruct the lagrangian of new physics, the process is the other way around and there is no direct mapping which can be simply estimated.

At LHC, there are tools like On Shell Effective Theories (OSETs), which characterizes the Hadron Collider data in terms of cross section and decay modes in case there would be a signature belong to a New Physics at TeV scale [13].

The purpose of this chapter is two fold. The first objective is to explore a conceptual problematization of interaction and materialization of quantum paradigm which is closely related to this dilemma. The integration of ideas, methods and data from diverse disciplines has been a transformative force in science so far, so the second objective is to give an idea on how to consider a toy model to the unified physics of quantum gravity and try to predict its consequences to be probed with on the LHC data.

In the upcoming chapters, the logic we go along will be seen after plunging into the model despite the reverse of this process would be possible once we got a signature at LHC as discussed in the last part.

CHAPTER 2

COMPACTIFICATION VIA LARGE EXTRA DIMENSIONS WITHIN ADD MODEL

The scenarios in the context of Large Extra Dimensions(LED), which aim to explain the origin of spacetime dimensionality can be classified in two distinct groups, Kaluza-Klein(KK) Theories and the Braneworld Theories. ADD Theory refers to the class of models, which incorporate the LED to our 3+1 minkowski space while localizing all the SM particles to our brane.

2.1 Kaluza Klein Theory

In the original theory of KK, U(1) local gauge invariance of electromagnetism was considered because of the circular geometry of the extra dimension. Concerning field theories, the action should be invariant under the symmetries of the theory in order to get equations of motions having those symmetries. Thus, in order to keep the lagrangian invariant up to the addition of a total derivative, a single scalar field is considered.

Considering the Electromagnetic field $A_\mu(x)$ where $\mu = 0, 1, 2, 3$, and representing the Gravitational field of Einstein with $g_{\mu\nu}(x)$ where $\mu, \nu = 0, 1, 2, 3$, the unification mechanism of Kaluza originally aimed to merge these two distinct fields with the metric $\hat{g}_{\mu\nu}$.

$$\hat{g}_{\mu\nu} = \begin{pmatrix} g_{\mu\nu} & A_\mu \\ A_\nu & \phi \end{pmatrix} \quad (2.1)$$

Here $g_{\mu\nu}$ corresponds to the graviton, A_μ and A_ν are photons and ϕ field stands for a *dilation* particle. As O.Klein suggested that this space would be spanned by the compactification scale L, which consists of compact dimensions given by a circle of radius R, a little circle is

implemented to an each point in the 4 dimensional Minkowski space as illustrated in figure 2.1(b).

For more than 1 spatial extra dimension, this space could be a higher dimensional sphere, a torus or some other manifold. Particularly in the original KK approach, the topology can be given by the direct product of the external manifold (4 dimensional Minkowski Space time) which is represented by M^4 and an internal manifold which corresponds to the compactified dimensions S^δ where δ denotes the number of extra spatial dimensions. Therefore $M^4 \times S^\delta$ should be the solution of the Einstein equations[14],[15] in this framework.

The KK theory in a nutshell, based on the assumption that, at distances larger than the compactification scale L , the extra dimensions should not be perceivable. However, at distances smaller than L they can be detected as illustrated in figure 2.1(a). Thus, the four dimensional space can be considered as a cylinder whose external 3 manifold is infinite, and the internal manifolds are constrained by z runs from 0 to $2\pi R$ with the circle of radius R out of perception[16].

$$\phi(x, z) = \phi(x, z + 2\pi R) \quad (2.2)$$

Then using a flat, positive metric $[+, -, -, -, \dots]$ we can start by writing the Lagrangian density,

$$\mathcal{L} = \frac{1}{2} \partial_A \phi \partial^A \phi \quad (2.3)$$

Here, the scalar field ϕ consists of four dimensional coordinates x^A where $A = \mu, 5$ and μ represents noncompactified spacetime coordinates $\mu = 1, 2, 3$

Due to the periodicity of the compactified dimensions, scalar field ϕ is also periodic with respect to $z \rightarrow z + 2\pi R$ therefore one can expand this field to the Harmonics of a circle considering one extra spatial dimension ($\delta = 1$).

$$\phi(x^\mu, z) = \sum_{n=-\infty}^{\infty} \varphi^n(x^\mu) e^{\frac{inz}{R}} \quad (2.4)$$

Rewriting the lagrangian by decomposing the scalar field into the eigenfunctions of the momentum,

$$\mathcal{L} = \frac{1}{2} (\partial_\mu \varphi \partial^\mu \varphi - \partial_z \varphi \partial_z \varphi) \quad (2.5)$$

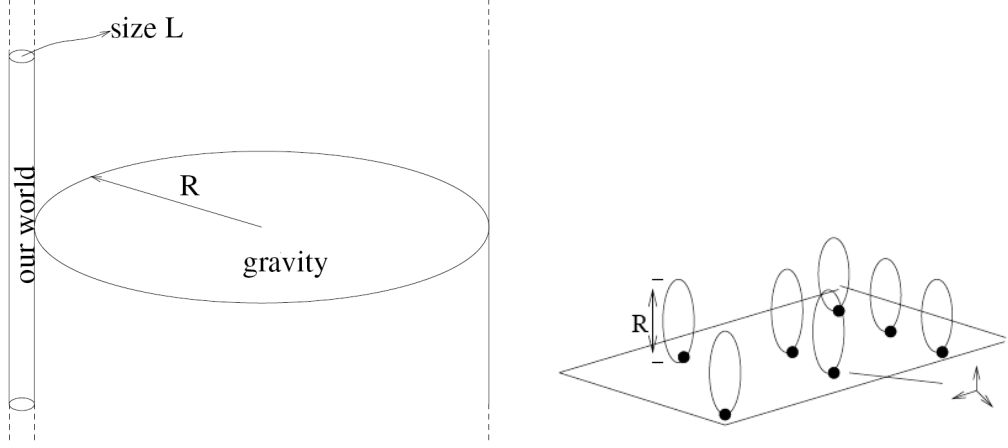


Figure 2.1: (a) KK Picture with gravity access to the whole space time, characterized by the spatial dimensions of R , where SM particles are confined on a subspace (internal manifold) whose compactification yields $L \ll R$. (b) Circles at each point in M^4 space.

Thus, as a 5 dimensional quadratic example on KK picture, 1 internal manifold can be implemented to the usual M^4 space as equation (2.4) is inserted into (2.5).

$$\mathcal{L} = \frac{1}{2} \sum_{n,m=-\infty}^{\infty} \left(\partial_{\mu} \varphi_n \partial^{\mu} \varphi_m - \frac{nm}{R^2} \varphi_n \varphi_m \right) e^{\frac{i(n+m)z}{R}} \quad (2.6)$$

Defining a discrete symmetry on the Minkowski space as S^1/Z_2 , the metric can be parametrized on S^1 and Z_2 orbifolding can be obtained after identifying $\Gamma : z \rightarrow -z$ function. Then plugging in the KK decomposition which containing (+) and odd (-) eigenfunctions, one can get

$$\phi(x^{\mu}, z) = \varphi_0^{+}(x^{\mu}) + \sum_{n=1}^{\infty} \varphi_n^{+} x^{\mu} \cos(nz/R) + \sum_{n=1}^{\infty} \varphi_n^{-} x^{\mu} \sin(nz/R) \quad (2.7)$$

Using 2.4 and 2.7, the degeneracy on KK mechanism can be revealed such that

$$\begin{aligned} \varphi_0^{+} &= \varphi_0 \\ \varphi_{n>0}^{+} &= \varphi_n + \varphi_{-n} \\ \varphi_{n>0}^{-} &= \varphi_n - \varphi_{-n} \end{aligned} \quad (2.8)$$

Choosing an odd (-) parity, orbifold symmetry removes half of the degrees of freedom on KK tower by mapping each circle to a finite length. This symmetry is actually used to project out the zero mode of the photon since $A_{\mu}(z) = -A_{\mu}(-z)$, but $\phi(z) = \phi(-z)$. Thus, $\varphi_n^{*}(x^{\mu}) = -\varphi_n(x^{\mu})$ relation can be used to remove the degeneracy on the KK tower and \mathcal{L} can be rewritten as,

$$\mathcal{L} = \frac{1}{2} \sum_{n=-\infty}^{\infty} \left(|\partial_{\mu} \varphi_n|^2 - \frac{n^2}{R^2} |\varphi_n|^2 \right) \quad (2.9)$$

$$\begin{aligned}
S &= \int d^4x \int_0^{2\pi R} dz \mathcal{L} \\
&= 2\pi R \sum_{n=-\infty}^{\infty} \int d^4x \frac{1}{2} \left(|\partial_\mu \varphi_n|^2 - \frac{n^2}{R^2} |\varphi_n|^2 \right)
\end{aligned} \tag{2.10}$$

which is nothing but a 4 dimensional action of infinitely many 4 dimensional fields. Ruling out the volume factor $2\pi R$ by substituting $\hat{\varphi}_n = \frac{1}{\sqrt{2\pi R}} \varphi_n$, one can get a canonically normalized field.

$$S = \frac{1}{2} \sum_{n=-\infty}^{\infty} \int d^4x \left(|\partial_\mu \hat{\varphi}_n|^2 - \frac{n^2}{R^2} |\hat{\varphi}_n|^2 \right) \tag{2.11}$$

Hence, the spectrum of the compactified theory consists of an infinite number of massive complex scalar fields with masses inversely proportional to the compactification radius.

2.2 Analogy with the ADD Model

In practice, the 5 dimensional picture with one of its dimensions compactified on a circle is indistinguishable from a 4 manifold mass spectrum, which gives rise to the Braneworld theories in subsequent years. In order to show the interface between KK mechanism and the ADD model for instance, we can start by writing the Schrodinger Equation for a free particle living on the slice of M^4 , when $L \gg R$.

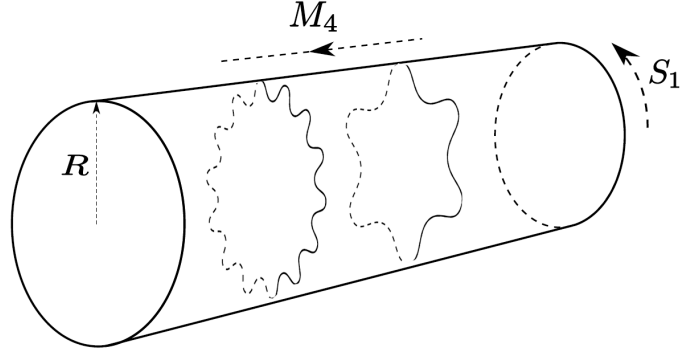


Figure 2.2: KK configuration of M^4 space, where nonzero modes propagate inside the cylinder

$$-\frac{\hbar}{2m} \frac{\partial^2}{\partial x^A \partial x^A} \phi(x^\mu, z) = E \phi(x^\mu, z) \tag{2.12}$$

Since $p^2 = \frac{2mE}{\hbar^2}$, $\phi(x^\mu, z)$ will be combination of planewaves propagating along μ

$$\phi(x^\mu, z) = e^{ip_\mu x^\mu} e^{ip_\mu z} \tag{2.13}$$

Then for an observer living on the 4 dimensional slice $L \gg R$, dispersion relation for massless particles can be written where $z = 0$

$$p_\mu p^\mu = 0 \quad (2.14)$$

Nevertheless, for an observer living outside the slice, $L \ll R$,

$$\left(-\frac{\hbar}{2m} \frac{\partial^2}{\partial x^A{}^2} + V(z) \right) \phi(x^\mu, z) = E \phi(x^\mu, z) \quad (2.15)$$

where $V(z) = 0$ for $0 < z < R$; or $V(z) = \infty$ for $z < 0$ and $z > \pi R$ Thus, 5th coordinate of momentum, p_5 is quantized as n/R and the dispersion relation turns out that,

$$p_\mu p^\mu - p_5^2 = 0 \quad (2.16)$$

$$p_\mu p^\mu - \left(\frac{n}{R} \right)^2 = 0 \quad (2.17)$$

Equation 2.17 corresponds to the KK tower including $n = 0$ homogeneous and $n \neq 0$ massive KK modes of spin-2, spin-1 and spin-0 fields. For instance, the energy in 4+1 dimension simply turns out that,

$$\begin{aligned} E^2 &= (p_\mu c)^2 + (p_n c)^2 + (mc^2)^2 \\ M &= m + n/R \end{aligned} \quad (2.18)$$

then $\sum n_i = N_{KK}$ will enhance the gravity at the compactification scale L by modifying the newtonian gravitational constant ($G_N = \frac{1}{M_{pl}^2}$) such that;

$$M_{pl}^2 = M_D^2 N_{KK} \quad (2.19)$$

Since the observer outside the slice sees the 5th coordinate as a conserved quantity, p_5 will be equal to M_D which is the effective scale, where gravity is modified because of the cumulative effect of the massive states of KK tower,

$$M_D = \frac{N_{KK}}{R} \quad (2.20)$$

substituting 2.20 on 2.19,

$$M_{pl}^2 = M_D^2 (M_D R) \quad (2.21)$$

and if there are δ number of extra spatial dimensions compactified on R ,

$$M_{pl}^2 = M_D^2 (M_D R)^\delta \quad (2.22)$$

2.3 Braneworld Theories

Despite the idea of living on a Braneworld is discussed in the context of General Relativity before, The earlier particle physics examples are given by Akama [17] and by Rubakov and Shaposhnikov [18] in 1980's. The size of the extra dimensions can be infinite in size in Braneworld models as a crucial feature which separates them from the KK Theories.

Essentially, everything is trapped in the 3-brane at low energies and the Einstein gravity is induced through the fluctuations of this 3-brane. With this approach, braneworld theories provide a way basically distinct from the compactification to hide the extra dimensions which become necessary to bypass the problem of renormalizability of the gravity.

Thus, our matter is localized on a 3D Hypersurface (Brane) which is embedded in a Higher dimensional space due to the fact that there is a potential well for particles, which is flat for our dimension. This potential well is sufficiently high so that the wavefunctions are boundstates.

Moreover the lowest eigenstate should have 4 dimensional mass being zero modes of bulk field, on the other hand, the excited states have 4 dimensional massive modes since they will be partners of our localized particles.

In field theory, the consequences of a symmetry may not be realized in the physical world as in the case of parity violation, therefore the lagrangian would contain some terms which do not obey this symmetry.

As a modification on the previous lagrangian density o 2.3, a prototype lagrangian with a symmetry breaking mechanism can be introduced [18].

$$L = \frac{1}{2} \partial_A \varphi \partial^A \varphi - V(\varphi) \quad (2.23)$$

where,

$$V(\varphi) = \frac{1}{2} \mu^2 \varphi^2 + \frac{\lambda}{4} \varphi^4 \quad (2.24)$$

Here $\varphi(z)$ is a single scalar field and λ is the dimensionless coupling constant corresponding the vacuum expectation value of this field. That is $\varphi(z)$ has two degenerate solutions being, $\varphi = v$ and $\varphi = -v$ as illustrated in the figure 2.3 [19].

Then the 5 dimensional action becomes,

$$S = \int d^4 x dz \left(\frac{1}{2} \partial_A \varphi \partial^A \varphi - \frac{1}{2} \mu^2 \varphi^2 - \frac{\lambda}{4} \varphi^4 \right) \quad (2.25)$$

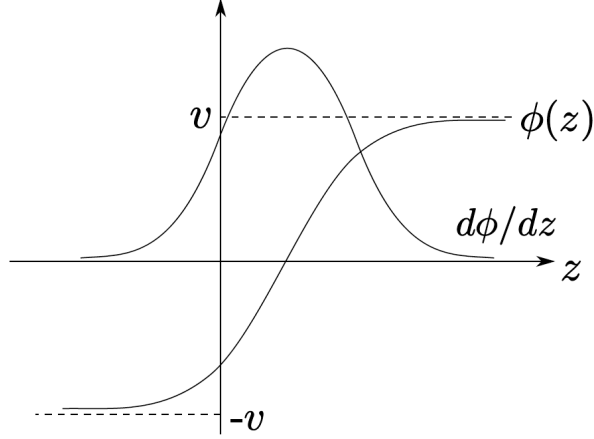


Figure 2.3: The solution interpolates between $\phi = V$ and $\phi = -V$ as extra coordinate z runs from $-\infty$ to $+\infty$

where $V(\varphi)$ yields the field equation,

$$\partial_A \partial^A \varphi + \frac{\partial V}{\partial \varphi} = 0 \quad (2.26)$$

Despite, the symmetry $\varphi \rightarrow -\varphi$ keeps the Lagrangian invariant under the Z_2 transformations, the vacua of the theory breaks this symmetry and forces φ field to sit one of the minimums on the figure 2.3. Then the solution of classical equation of motion coincides with so called *Kink* or a *Domain Wall* solution depending only on the extra coordinate denoted with $\varphi_c(z)$.

The analytic expression of domain wall solution can be rewritten,

$$\varphi_c(z) = v \tanh(\sqrt{2\lambda} v z) \quad (2.27)$$

Hence, there is no translational invariance along z direction and the 5D Lorentz invariance is spontaneously broken by this domain wall.

Furthermore, since this domain wall can be anywhere on the extra coordinate z , shifting it requires an additional kinetic energy that can be obtained from the excitations of the classical solutions, where scalar modes of the field occur. This excitations living on the brane world volume is identified as SM particles so the following decomposition can be made,

$$\varphi(x, z) = \varphi_c(z) + \delta\varphi(x, z) \quad (2.28)$$

Therefore, there will be bound states in the presence of this wall yielding the linearized field equation.

$$\partial_A \partial^A (\delta\varphi) + \frac{\partial^2 V}{\partial \varphi^2} [\varphi = \varphi_c] \cdot \delta\varphi = 0 \quad (2.29)$$

which can be written as:

$$\partial_\mu \partial^\mu - \partial_z^2 (e^{ip_\mu x^\mu} \delta\varphi_m(z)) - \mathcal{U}(z) \delta\varphi = 0 \quad (2.30)$$

So the equation turns into the precise form of the Schrodinger Equation in a potential well where

$$\mathcal{U}(z) = \frac{\partial^2 V}{\partial \varphi^2} [\varphi = \varphi_c] \quad (2.31)$$

Writing the dispersion relation on the 5th coordinate gives massive modes similar to the KK case and the eigenvalues of the Schrodinger operator corresponds to m^2 ($p_\mu p^\mu = m^2$)

For $n = 0$ eigenvalue, there is a zero mode $m^2 = 0$ which is the simplest realization of the Braneworld scenario for massless particles.

Note that, regarding the massless mode solution, the vibrational mode of the kink splits into discrete and continuum modes where discrete ones correspond to the excited states while continuum modes correspond to the particles moving freely away from the brane.

2.4 Reconciling Compactification on Braneworld: ADD Scenario

Rather than worrying about the inconvenient size of the Plank length which is impossible to probe, Arkani-Hamed, Dimopoulos and Dvali (ADD) proposed an alternative to supersymmetry (SUSY) to solve hierarchy problem at EW scale [20]. This new framework opened up new possibilities to eliminate the Higgs mass hierarchy problem and moreover this compactification scenario could also be embedded in String Theory [21]. Therefore this model is considered as a toy model to the string theory where chiral gauge fields are confined to a reasonably simple brane configurations [22].

The model considers $M^4 \times K^\delta$ spacetime symmetry where SM particles are localized on the 4 dimensional Minkowski space M^4 while gravitons freely propagate along $4 + \delta$ dimensions as illustrated in the figure 2.4

In order to obtain 4 dimensional gravity on a brane, the braneworld idea is combined with the compactification in such a way that SM particles are confined on the 3-brane, while gravity spreads to $4+\delta$ dimensions. Thus, ‘Compactification mechanism of KK Theory solves the problem of gravity while localizing all other fields on the domain wall solves the hierarchy problem’ [23]. The other consequences of the ADD Theory can be summarized as follows.

- The brane width is taken to be zero instead of M_D^{-1} .

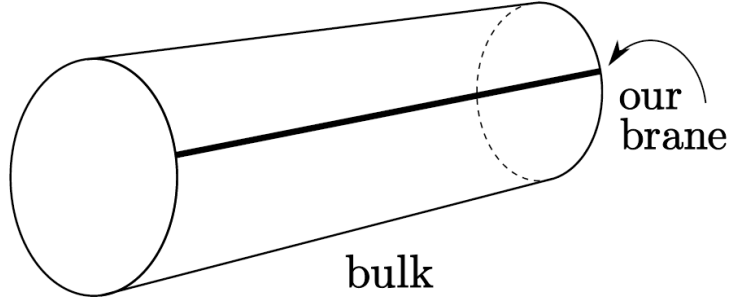


Figure 2.4: The solid line represents our *Braneworld* where only gravity can live on the bulk

- ▶ Brane Fluctuations are neglected.
- ▶ All Extra Dimensions have equal size of R .
- ▶ Only Gravity can propagate in the bulk.

In the most basic version, δ extra spatial dimensions are compactified on a torus with common circumference R , and the considered brane will extend through the infinite spatial directions. It should be also noted that, the brane considered in the ADD framework should have a very small tension (energy per unit volume) not to warp the extra dimensional space.

Then the action of ADD model takes the form [16]:

$$S_{ADD} = \frac{M_D^{2+\delta}}{2} \int d^4x \int_0^{2\pi R} d^\delta z \sqrt{G} R_{4+\delta} + \int d^4x \sqrt{g} (T + \mathcal{L}_{SM}(\Psi, M_{SM})) \quad (2.32)$$

where G and g are gravitational and gauge couplings respectively, T denotes the tension of the brane $T = \int dy H(\varphi_c)$ and Ψ is a 5 dimensional dirac fermion.

In order to derive the consistency equation 2.22 with the action method, we can start by writing the fundamental action for gravity where $D = 4 + \delta$ for $L \ll R$,

$$S_G = \frac{1}{16\pi G_D} \int d^4x \int R^{(D)} \sqrt{g^{(D)}} d^4x d^\delta z \quad (2.33)$$

At large distances only homogeneous modes will be relevant such that $g_{\mu\nu} = g_{\mu\nu}(x)$. Substituting this into 2.33 at $L \gg R$, one can write the effective action on the 4D minkowski space.

$$S_{eff} = \frac{V_N}{16\pi G_D} \int R^{(4)} \sqrt{g^{(4)}} d^4x \quad (2.34)$$

Here, G_4 is 4 dimensional gravitational coupling (Newton Constant) which is $G_4 = \frac{G_D}{V_\delta}$ where $V_\delta = (2\pi R)^\delta$ if all extra dimensions are compactified with a common circumference. Thus,

Table 2.1: Number of Extra Dimensions vs. Compactification Radius

δ	R(mm)
1	10^{16}
2	1
3	$5 \cdot 10^{-6}$
4	10^{-8}
5	10^{-10}

$G_4 = \frac{1}{M_{pl}^2}$ and $G_D = \frac{1}{M_D^{2+\delta}}$ can be written when $r \sim R$,

$$\begin{aligned} \frac{G_4}{r} &= \frac{G_D}{r^{\delta+1}} \\ M_{pl} &= M_D \cdot (M_D R)^{\delta/2} \end{aligned} \quad (2.35)$$

which is consistent with the equation 2.22

2.4.1 Constraints on the Parameter Space

Despite the the current experimental limits of ADD Model is given in chapter 6, one can infer the consequences by taking a quick look at the consistency Equation 2.22 and Equation 2.35,

In Table 2.1, it can be immediately seen that the radius of compactification is getting reduced with the increasing number of δ . Here, $\delta = 1$ corresponds to the astronomical distances which can be excluded with indirect measurements. But for the higher δ values ,the limits of present tests are still valid.

Constraining the radius of compactification to the millimeter scale $R > 0.1\text{mm}$, there appears sensible values for M_D scale, only for $\delta = 1$ and $\delta = 2$ cases. For the case $\delta = 2$, $M_D \lesssim 10$ TeV the model is interesting from the hierarchical point of view. For $\delta = 3$, M_D is constrained to lie below few GeV, which is phenomenologically ruled out. Higher values of δ in this case become more and more unacceptable.

Hence, $\delta=2$ seems to be the most viable possibility, which would solve the hierarchy problem and compatible with the center-of-mass energies applicable at LHC. Nevertheless, $\delta =2,3,4$ cases are also considered in this thesis by taking into account a deeper symmetry or mechanism removes the finite vacuum energy, associated with a different compactification. For the cases where $\delta =5$ or $\delta =6$, the signal is not strong enough to be detected in a pure perturbative regime[24].

CHAPTER 3

LHC AS A NEW FRONTIER OF PHYSICS

3.1 Overview to Large Hadron Collider

The Large Hadron Collider (LHC) is a 26.7 km circumference proton-proton accelerator carried out at CERN operating as a giant physics lab on the Swiss-French border. Since November 2007, the collider's circle has completed installation in the old tunnel of Large Electron Proton Collider (LEP). Then on 30 March 2010, the first planned collisions took place between two 3.5 TeV beams setting a new world record for the highest-energy man-made particle collisions even if it has reached only the half of its designed center of mass energy.

Once fully operational, the LHC will provide collisions between proton beams at a luminosity exceeding $10^{33} \text{ cm}^{-2} \text{ s}^{-1}$. It will also operate with Heavy Ion (Pb-Pb collision) beams with a lead nuclei at an energy of 574 TeV ($92.0 \mu\text{J}$) per nucleus.

There are four main experiments take place at the LHC: two general purpose detectors, ATLAS and CMS, and two dedicated detectors, ALICE and LHC-b which will study heavy ion physics and B-physics respectively. Figure 3.1 shows the four experimental sites along the LHC ring where the CMS detector situated approximately 100m underground taking data from both the p-p and Pb-Pb collisions.

3.2 Luminosity Challenges

Reaching the high energy scale by increasing the luminosity will provide a good opportunity to test Higgs and BSM models based on the advantage of looking at the decay modes of heavier particles. In return, the combination of very high field magnets and very high beam intensities required to reach this luminosity targets, makes operation of the LHC a great challenge [25].

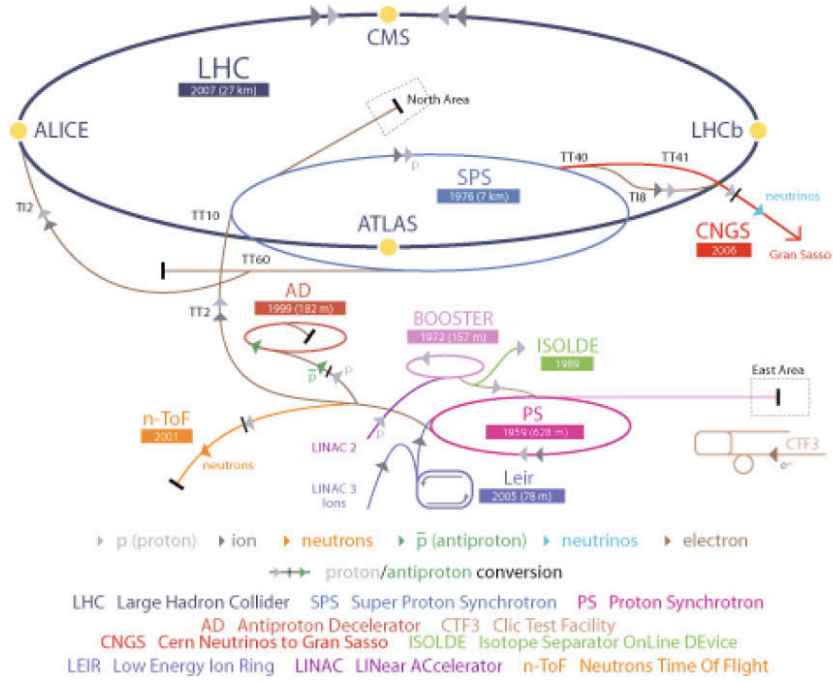


Figure 3.1: LHC Complex

In electron-positron colliders, the particles lose an amount of energy much larger than the stored beam energy in every second through synchrotron radiation. This loss must be continuously compensated by the RF system, and as a consequence, this phenomenon limits the attainable energy while damping of particle oscillations. These effects are unimportant at LHC since the energy loss of heavy particles like protons is proportional to $\frac{1}{m^4}$ due to the synchrotron radiation, where m is the mass of the particle. Thus, the energy radiated during the same time is only a tiny fraction of the beam energy, becoming significant at only much higher energies (~ 100 TeV).

In Contrast to CDF and $D\phi$, currently operating in Fermilab, The LHC produces pp collisions instead of proton-antiproton collisions, since it turns out to be technically difficult to produce sufficient amount of antiprotons needed to achieve design luminosity of LHC.

The difficulty is that, protons are not fundamental particles and the initial state of interacting partons is not precisely known. Moreover, in order to achieve the high luminosity goal, $\sim 10^{11}$ protons are squeezed into bunches collided at each 25 nano second (ns). Because of this large number of protons, the average number of inelastic pp collisions per bunch crossing is high, up to 20 for the design luminosity. This leads to increasingly more difficult experimental conditions, since the rare interesting events may occur in a bunch crossing

Table 3.1: Important parameters at LHC

Parameter	Value
Maximum c.m (\sqrt{s})	14 TeV
Circumference	26.659 km.
Operating temprature of Dipole	1.9 K
Nr. of Dipoles	1232
Nr. of Quadrupoles	858
Nr. of Correcting Magnets	6208
Nr. of RF cavities	8/beam
Peak Magnetic Dipole Field	8.33 T
Minimum Distance between bunches	7 m
Design Luminosity	$10^{34} cm^{-2} s^{-1}$
Nr. of bunches per beam	2808
Bunch spacing	25ns
Nr. of protons per bunch	$1,1510 \cdot 10^{11}$
Nr. of collisions per crossing	~ 22

superimposed on the top of these 20 minimum bias events [26].

The event rate N for a physics process with sigma cross-section is proportional to the Collider Luminosity which can be written as a function of n_1 and n_2 particles per beam at a given revolution frequency.

$$N = L\sigma \quad (3.1)$$

$$L = k \frac{n_1 n_2 f}{4\pi\sigma_x \sigma_y}$$

Taking $n_1 = n_2$, one can use N^2 where n is the nominal number of protons per bunch around 1.1510^{11} and f being the revolution frequency taken around $\sim 11.25kHz$ and k is the number of bunches ~ 2808 . (σ_x, σ_y) are the beam sizes at the collision point (horizontal, vertical) ~ 16 meter. The other relevant parameters of the LHC is given in the table 3.2.

$$-\Delta E = \frac{4\pi\alpha}{3R} \beta^3 \gamma^4 \quad (3.2)$$

where $\beta = v/c \sim 1$ and $\gamma = \frac{E}{mc^2}$

The collision process is also getting complicated since synchronizing two proton beams in the same field is not possible. In order to make counter rotating possible, the sign of the field is changed and the beams remain in separate vacuum chambers (in the bending sections) with opposite B field direction. Thus in fact we actually have two LHC machines side by side.

A small beam size is required in order to squeeze the number of particles in a small phase volume. Reaching the LHC design luminosity requiring a small transverse beam profile, a high bunch collision frequency and a large number of particles per bunch is considered. Beam behavior is generally studied by measurement of the beam size using a stark camera. The effect of electron-clouds and beam-beam interactions on the vertical beam size is examined in the beam collisions so the beam size can also be measured by a single positron beam [27].

At a center of mass energy around 200 GeV, synchrotron radiation caused most of the energy that was added to the beam in the radio frequency (RF) cavities to be radiated off again, thereby setting an upper limit to its energy reach. LHC clearly needed more energy to carry out to foreseen energy physics programme. In order to avoid the synchrotron radiation, there are two possibilities: one could increase the radius of the collider (optimally reaching a linear collider) or one could increase the mass of the accelerated particle. This can be seen from the formula below for synchrotron energy loss of high energy particles 3.3:

$$\sigma_{ll} = (\beta' \epsilon)^2 \quad (3.3)$$

where β' is the beam envelope varies along the ring at the collision points and ϵ is the phase space volume occupied by the beam.

3.3 CMS(Compact Muon Solenoid) Detector

The CMS Detector operates at LHC-CERN, which is conceived to study p-p collisions at a centre-of-mass energy of 14 TeV and at luminosities up to $10^{34} \text{ cm}^{-2} \text{ s}^{-1}$. A highfield superconducting solenoid surrounds a silicon tracker, an electromagnetic calorimeter, and a hadron calorimeter. The return yoke is instrumented with muon detectors covering most of the 4π solid angle. Forward sampling calorimeters extend the CMS pseudorapidity coverage at high η values.

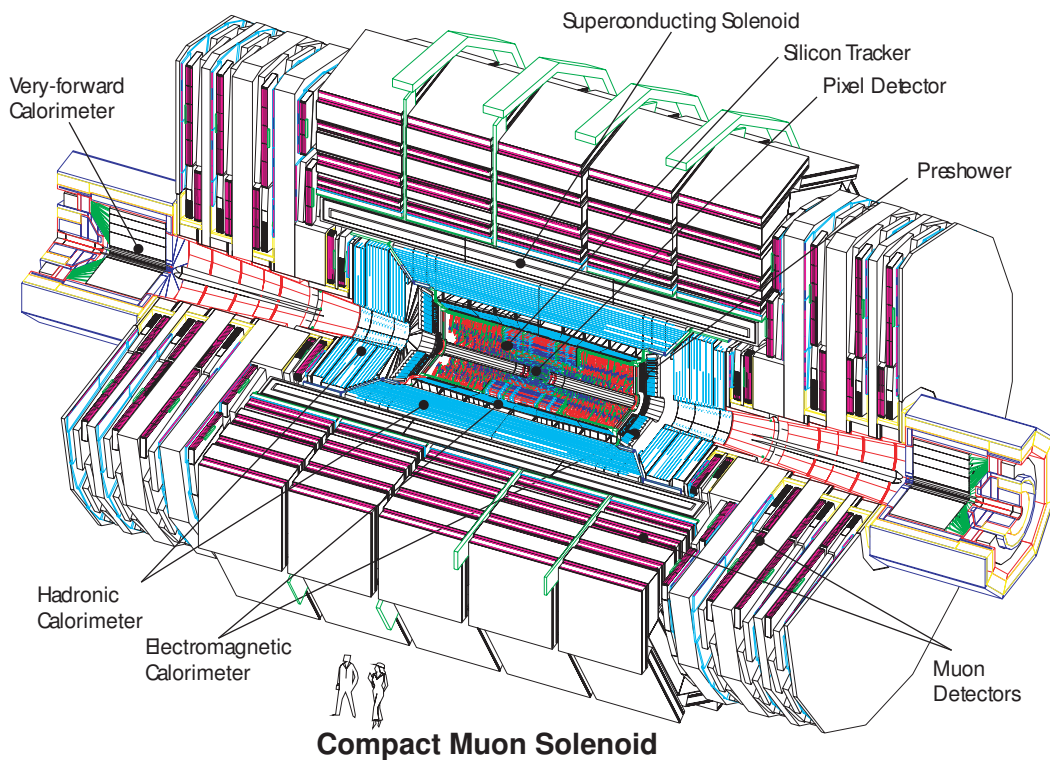


Figure 3.2: CMS Overview

It has been designed to detect the diverse signatures of new physics at the Large Hadron Collider given in Figure 3.2. It will do so by identifying and precisely measuring muons, electrons and photons over a large energy range by determining the signatures of quarks and gluons through the measurement of jets of charged and neutral particles (hadrons) with moderate precision. Then inferring the missing transverse energy flow will enable the signatures of non-interacting new particles as well as neutrinos to be identified [28].

In order to achieve these goals, the decay remnants should be identified and their mo-

Table 3.2: Parameters of the CMS Superconducting Solenoid

Field	4T
Inner Core	5.9 m
Length	12.9 m
Number of Turns	2168
Current	19.5 kA
Stored Energy	2.7 Gj
Hoop Stress	64 atm

mentum has to be measured as precisely as possible. To measure the momentum of charged particles, which hardly leave any energy in the calorimeter, a high magnetic field of 4 tesla is applied and the curvature of tracks is measured. CMS chooses a large superconducting solenoid, where the parameters of which is given in table 3.3.

The following coordinate system is used: The x-axis points radially inwards towards the center of LHC, and the y-axis points vertically upwards. Thus, the z-axis points along the beam line from LHC point 5. The azimuthal angle ϕ is measured from the x-axis in the x-y plane. The polar angle θ is measured from the z-axis. The transverse momentum and energy are denoted p_T and E_T , respectively. The definition of the pseudorapidity is given in 3.4

$$\eta = -\ln\left(\tan\frac{\theta}{2}\right) \quad (3.4)$$

In the relativistic limit, pseudorapidity behaves like rapidity and this variable is preferred to θ since the difference between the rapidity of two particles is invariant under a Lorentz boost.

3.3.1 Interaction of Particles with Material

The particles interact with the material in the CMS detector with the following way.

- ▶ High energetic photons do not interact with any detector component until they decay into a electron positron pair, leading to an electromagnetic shower. This process would occur in tracker, but often in ECAL.

- ▶ Electrons leave a single track in the tracker pointing to the part of the ECAL, and deposit their energy to this calorimeter just like photons.

- ▶ Muons leave a track in the tracker but only about 4 GeV of their energy, which can be deposited in the calorimeter. In many cases they only interact with the muon system.

- ▶ Jets are originated from gluon radiation or quarks. They leave a signal in the inner tracker as well as in the ECAL. However, most of the energy is deposited in the HCAL.

► Weakly interacting particles like neutrinos or a possible graviton would leave no signal in the detector. If these particles also have a large momentum, a transverse momentum imbalance can be inferred from the negative sum of all measured transverse momenta, which is represented with ME_T .

CMS detector is cylindrical and has a length of 30m, a radius of 7.5 m with a total weight around 12500 tons. The larger sub-detectors are, starting from the center: The tracker, ECAL (Electromagnetic Crystal Calorimeter), HCAL(The hadronic metal-scintillator calorimeter), The superconducting solenoid coil and the muon drift chamber system.

3.4 The Tracker

This part of the detector is the world’s largest silicon detector. It has 205 m^2 of silicon sensors (approximately the area of a tennis court) comprising 9.3 million micro strips and 66 million pixels. This is necessary to study B-hadron physics including CP-violation, BS oscillations and rare B-decays right after the start of the experiment [29].

In the high luminosity regime, about 20 collision per bunch crossing are expected to produce more than 1000 charged particles in the acceptance of the tracker. Finally segmented silicon sensors (strips and pixels) enable charged particles to be tracked and their momenta to be measured. They also reveal the positions at which long-lived unstable particles decay.

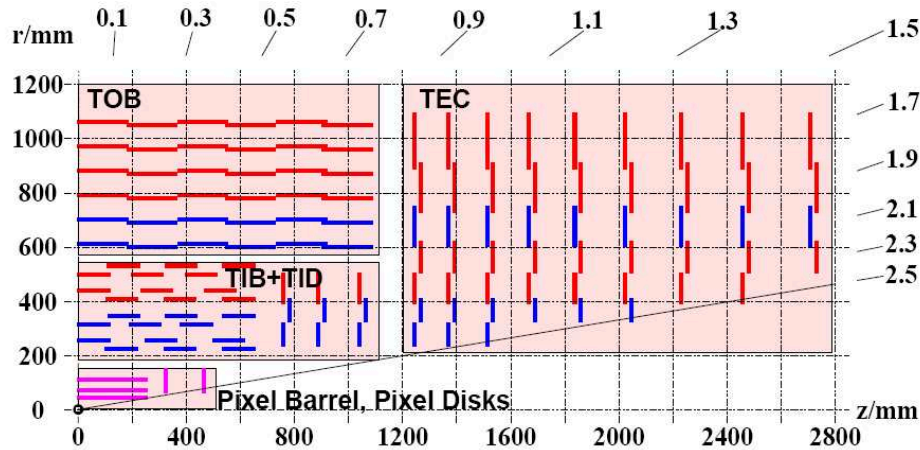


Figure 3.3: CMS tracker layout

An overview of the CMS tracker layout is given in Figure 3.3. The tracker is subdivided into four silicon strip sub detectors, namely the Tracker Outer Barrel (TOB), the Tracker

Inner Barrel (TIB), the Tracker Inner Disk (TID), the Tracker Endcap (TEC), and two silicon pixel sub detectors, the pixel barrel and the pixel disks. All active components are housed in a cylindrical volume with a length of 5.4 m. and a diameter of 2.4 m. In order to protect the silicon detectors from thermal runaway due to increased leakage current from radiation damage in the hostile LHC environment, the full silicon tracker needs to be operated at -10 degrees of Celcius and thus in a dry environment for years. An active thermal shield placed outside of the tracker volume provides isolation, and a cooling system extracts the heat from the 60 kW power dissipation generated by the front-end electronics [30].

Compared to ATLAS, the magnetic field of CMS tracker is rather large, which allows for good lepton and photon reconstruction and identification efficiencies. It further allows to correct jets using the particle flow technique.

3.5 ECAL

The Electromagnetic Calorimeter is placed around the tracker. The function of the electromagnetic calorimeter is to measure the energy of electrons and photons and, together with the hadron calorimeter, to measure jets with high precision. The design of the CMS electromagnetic calorimeter is driven by the requirement to provide an excellent di-photon mass resolution for the crucial two photon decay mode of the higgs boson $H \rightarrow \gamma\gamma$ which is the main Higgs discovery channel for m_h smaller than 130 GeV.

There are 36 identical supermodules, 18 in each half barrel, each covering 20 degrees in ϕ . The barrel is closed at each end by an endcap. In front of most of the fiducial region of each endcap is a preshower device. Figure 3.4 shows a transverse section through ECAL [31].

The mass resolution depends on the resolution in energy of two photons and the error of the measured angle between them. The energy resolution of the ECAL can be parametrized as

$$\left(\frac{\sigma}{E}\right)^2 = \left(\frac{a}{\sqrt{E}}\right)^2 + \left(\frac{\sigma_N}{E}\right)^2 + c^2 \quad (3.5)$$

where the first term is the stochastic term, due to fluctuations of the shower containment and to photo-statistics, the second term is the noise term, consisting of both electronics noise and the pile up energy, and c^2 is the constant term where the coefficients of a and c are determined by the active detector material.

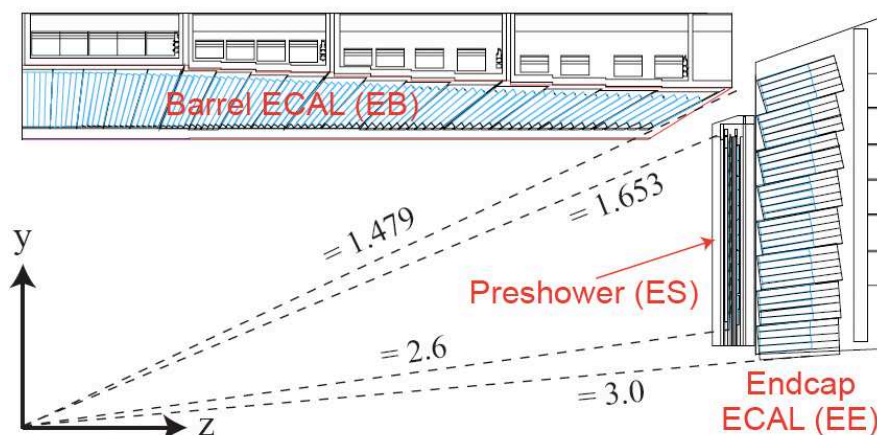


Figure 3.4: Transverse section through the ECAL, showing geometrical configuration.

In order to achieve a good energy resolution, all the contributing terms have to be kept small and should be of the same order at the relevant photon energies. The CMS collaboration has chosen lead tungstate ($PbWO_4$) crystals for the electromagnetic calorimeter ECAL because of their excellent energy resolution. Apart from high resolution and fast response, the ECAL and its read-out electronics need to be resistant against radiation damage caused both by the charged particles and by neutrons. A design that fulfills all requirements consists of about 80000 lead tungstate $PbWO_4$ crystals. A high density and a short radiation strength with a small Moliere radius are the main reasons to choose this material allowing for a compact ECAL design with narrow showers. There are 2 main reason to choose lead tungsten:

- ▶ Scintillating process is fast matching the LHC bunch crossing time of 25ns.
- ▶ The material is intrinsically radiation hard. Together with the choice of this material above, the constants in the formula are $a = 2\%$ and $c = 0.55\%$

A constant term is required in order to benefit from $PbWO_4$ crystals effectively in the energy range relevant for the Higgs search. The challenging goal of keeping it very small can be reached if the inter calibration between crystals would be kept in precision. This puts severe requirements on the control of the temperature stability (cooling system) with a following radiation damage.

3.6 HCAL

The Hadron Calorimeter (HCAL) is designed to measure the timing, angular direction and energy of hadronic showers for reconstructing jets and missing transverse energy, and by calorimetric triggers. It also contributes to the identification of electrons, photons and muons through complementing the measurements by the ECAL and the muon system.

The CMS central HCAL is a scintillator-based sampling calorimeter. It has thin layers of scintillator interleaved between brass absorber plates. To maximize the absorber thickness in the small available space (about 1 meter radially) the brass plates are kept relatively thick (~ 5.5 cm) and the scintillator is relatively thin (3.8mm).

One of the tasks before us while designing the CMS Hadron Calorimeter (HCAL) is the selection of the front-end signal preparation. The central part of the HCAL uses a photon detector and digitizing electronics. The choice/design of the photon detector and front-end electronics are very tightly tied together. The front-end electronics has to accommodate the sensitivity, capacitance, shaping, and other properties of the photon detector. In the development of the HCAL these two tasks of developing the front-end electronics and the photon detector were constructed in parallel.

The CMS Hadron Calorimeter organized into 4 subsystems contains 9072 readout channels. The barrel (HB, 2592 ch.) and endcap hadron calorimeters (HE, 2592ch.) use scintillator as the active medium and are located in the central detector. The very forward calorimeter (HF, 1728 ch.) consists of a Cerenkov radiating quartz fiber, is located in the forward region outside of the magnetic field volume. The central HCAL sits inside the CMS solenoidal superconducting magnet. The final region the outer calorimeter (HO, 2160 ch.) sits outside the central magnet and like the central calorimeters, it has a scintillator too as the active medium. Figure 3.5 shows the relative placement of the HB, HE, and HO.

The support and control of all components of HCAL is performed by the HCAL Detector Control System (DCS) infrastructure includes many subsystems for control and monitoring.

This system as a whole allows to set and monitors at high and low voltages, downloads the parameters for the frontend electronics, controls the charge injection for electronics calibration, monitors the temperature of the on-detector readout boxes, monitors the forward calorimeters for radiation damage, and controls the LED, laser and radioactive source calibration systems.

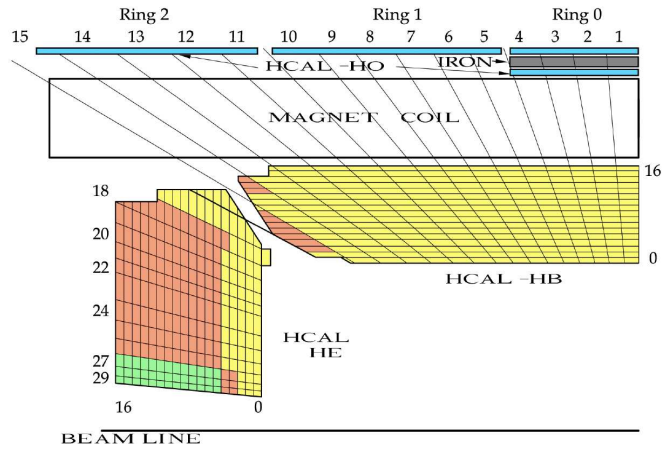


Figure 3.5: Layout of HCAL Barrel and Endcap detectors. Inner phi segment of a wedge.

3.6.1 HCAL Partitions

HCAL is logically separated into 120° sections, corresponding to independent trigger regions. These partitions are implemented using the JCOP Framework State Machine Interface (SMI). Because of the DAQ hardware structure, the partitioning could only be accomplished one level below the HCAL DCS Supervisor. The detector partitioning is set in part by the master clock fan-out from the trigger timing and control (TTC) system and the HTR layout, which is designed to accommodate the level-1 trigger. The HCAL consists of 5 partitions:

- ▶ Three sectors of the HB together with the endcap HE calorimeter covering 120° degrees in ϕ . Each of these sectors has subpartitions HE-, HB-, HB+ and HE+. HB covers the pseudorapidity range up to $|\eta| < 1.4$ with 36 identical azimuthal wedges ($\Delta\phi = 20^\circ$) form the two half barrels while HE covering $1.3 < |\eta| < 3.0$ which have inner radii of 0.4 m and outer radii of 3m. Each HE consists of 14 η towers, where the first tower overlaps with HB.

- ▶ Similarly HF having plus and minus sides as sub-partitions covers $3 < |\eta| < 5$ aim to measure high energy forward jets and complete the hermetic coverage for a better E_T determination.

- ▶ Tail catcher HO having 5 sub-partitions HO2-, HO1-, HO0, HO1+ and HO2+ covering $|\eta| < 1.26$ region and increases the effective thickness of HCAL.

Each sub-partition is also subdivided into readout boxes (RBXs) each of which is further into 4 readout modules RM. The infrastructure elements such as radioactive source server or HV system server, etc. could not be partitioned and belong HCAL DCS as a whole. Hcal

Partitioning is illustrated in figure 3.6.

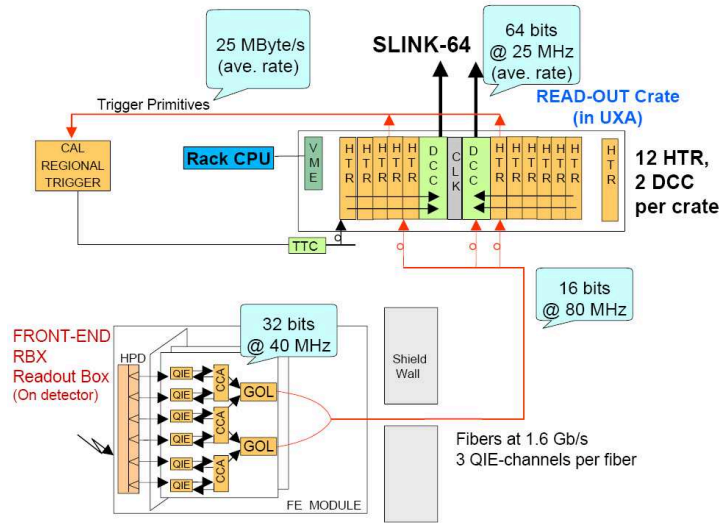


Figure 3.6: HCAL Partitioning

The high magnetic field where the HCAL is located caused a severe limitation on the choice of photodetector. Actually no suitable photodetector existed and it is forced to be developed a pixilated proximity-focused HPD. The readout of the calorimeter channel requires just 7 bits of data rather than 14 bits so a linear single range readout is sustained. The data compression reduces front end power requirements and minimizes cable volume leaving the detector.

3.7 The Muon System

Many interesting processes considered in the BSM context such as SUSY or Extra Dimensions as well as SM processes related to EW, Higgs or B Physics give rise to final states enriched with muons granting significant part of discovery and precision measurements at LHC. Since muons are minimal ionizing particles, they are very penetrating as long as their energy is sufficient not to be bent by the magnetic field through the solenoid. Muons are heavy particles (~ 105 MeV) so they live relatively long ($\tau = 2,2 \cdot 10^{-6}$ s) in which they don't emit bremsstrahlung radiation as electrons.

The muon system cover the region $|\eta| < 2.4$ and split into a central (MB) and two forward (ME) parts. 4 disks are installed for both of these endcaps and they are separated by the iron return yoke, which absorbs the bremsstrahlung photons, electron positron pairs and hadronic

punch throughs. Figure 3.7 shows the side view of CMS comprising Endcap muon system (ME) and the central barrel part (MB).

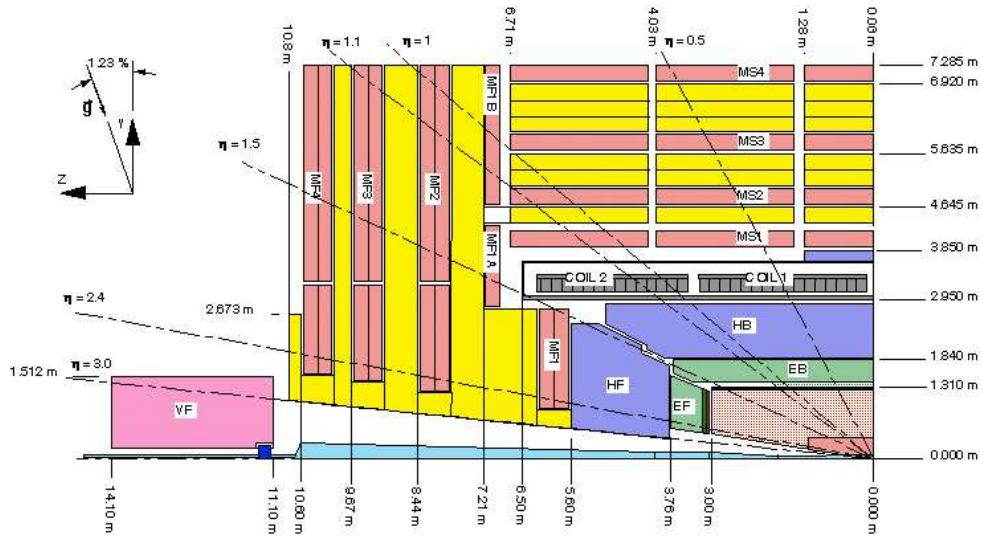


Figure 3.7: Side view of MB and ME Muon systems

The central part covers $|\eta| < 1.2$ range and the muon rates are expected to be rather small since the drift tube (DT) chambers are used as a tracking device. In the endcaps, muon rates are getting a bit higher, led to the choice of Cathode Strip Chambers (CSC). They have a very good time resolution to identify the correct bunch crossing despite the position resolution is a bit poor compared to new progress.

In the inner tracker region, momentum measurement of low energetic muons are made. Considering high energetic muons, energy loss and multiple scattering can be neglected and the combinations of the measurements made in tracker and outer muon system make it possible to measure the curvature of the track properly. It doesn't effect the resolution of the momentum measurement but increases the probability to determine charge of muons above 1 TeV energy scale.

CHAPTER 4

CMS TRIGGER SYSTEM

4.1 Introduction

Before starting to discuss the Trigger Infrastructure at CMS in detail, it would be convenient to mention about offline and online computation issues for the first reader. The online computation requires real time data processing, where the decisions are irreversible and the data cannot be recovered. However, an offline computation does not require real time data processing therefore the decisions can be reconsidered for the event filtering and other detailed selections and the most importantly, data can be reprocessed [32].

The trigger is the start of the physics event selection process where in every 25 ns, a further decision has to be made. It requires only a small subset of the detector data processed rapidly with very little dead time for all channels. It performs the the data acquisition as a consequence via allowing or rejecting the event processing.

Regarding the nominal LHC design luminosity of $10^{34} \text{ cm}^2 \text{ s}^{-1}$, every bunch crossing gives rise to an average of 17 events. So the input rate of 10^9 interaction per second must be reduced by a factor of 10^7 to 100 Hz, which is the maximum rate that can be achieved by the online computer farm in general.

In order to achieve this data reduction, CMS uses a 2 layer event filtering mechanism, namely

- ▶ Level 1 Trigger System
- ▶ High Level Trigger (HLT) system.

All data is stored for $3.2 \mu\text{s}$ in the first phase, after which no more than 100 kHz of the stored events are forwarded to the High Level Triggers.

4.2 Requirements of the Trigger System

4.2.1 Physics Requirements

The data sets to be taken are determined by CMS Physics priorities based on the identification of muons, electrons, photons, jets and missing transverse energy. The trigger efficiency should be reasonably high correspond to a lower cut with respect to the specific type of the particle in question.

The trigger system should be capable of selecting leptons and jets over the pseudorapidity range $|\eta| < 2.5$, with an efficiency which is very high, above a selected threshold in transverse momentum.

Single and multiple jet triggers are required with a well defined efficiency over the entire rapidity range $|\eta| < 5$, so the reconstruction process of jet spectra overlaps with the attainable data. Jet triggers are expected to be fully efficient in response to the high transverse momenta events. Regarding the missing transverse energy trigger, a threshold around 100 GeV is generally considered.

Note that the L1 p_T cutoffs are, and ought to be, somewhat smaller than the offline physics analysis cuts. The reason for such a requirement is that the efficiency turn-on curves for the L1 trigger will be somewhat softer than can be achieved with a full analysis including the best resolutions and calibration corrections.

The enormous range of the cross sections makes the triggering at LHC a very challenging task. The trigger system has to select efficiently a few interesting events among millions of background ones.

Another crucial task at the LHC is triggering the enormous range of cross sections belong to different phenomenological studies. The interesting events should be selected effectively in parallel to the physics channel studied. The trigger simulation is performed by PYTHIA or ISAJET programs using integer scales with appropriate bit resolutions and dynamic ranges implemented in the hardware. N-tuples generated from this trigger simulation of the QCD jet events are used to make integrated trigger rate plots versus the E_T values for various trigger channels and combinations. The ORCA simulated trigger data and the PYTHIA Monte Carlo generator information are used together to obtain the trigger efficiencies as a function of generated trigger particle momenta.

4.2.2 System Requirements

The trigger has to be inclusive, local, measurably efficient, and fill the DAQ bandwidth with a high purity stream. The local philosophy of the trigger implies an initial trigger selection of electrons, photons, muons and jets, which relies on local information tied directly to their distinctive signatures, rather than on global topologies. For example, electron showers are small and extremely well defined in the transverse and longitudinal planes. Information from a few ECAL and HCAL calorimeter towers (at the L1 trigger), the preshower detector, and a small region of the tracking volume (at higher trigger levels) are sufficient for electron identification.

The Trigger Architecture would be tuned in 3 ways to measure lepton and jet efficiency.

- ▶ In the case of overlapping programmable triggers, multiple triggers with different thresholds and cuts run in parallel to each other.

- ▶ Presecaled Triggers contains a secondary lower threshold cut which runs in parallel to the strict triggers.

- ▶ Prescaling of a Particular Trigger by removing one of the simultaneous cuts.

As a result, the online thresholds in the selections should be consistent with those of the offline and the events must be selected carefully in order to keep the permanent storage media in balance.

4.2.3 Rate Requirements

Since the L1 trigger rate is limited by the speed of the detector electronics, the readout and the rate which is processed by DAQ system is also constrained by the design capability of the readout, event builder and event filter at 100kHz. However, in startup conditions, this maximum capability will not be required and reduced to the 75 kHz with the implementation of new Event Filter. In addition to that, the uncertainties in estimations of cross sections at high energies and limited knowledge of branching ratios also impose a large error on the estimated trigger rates.

4.2.4 Structural Requirements

The time between beam crossings at the LHC is 25 ns, which is too short to read out the megabytes of data for each event causes a crucial trigger decision. The data are therefore stored in a pipeline and the first level trigger decision is transmitted to the detector electronics

within $3.2 \mu s$ after the crossing. In order to avoid the deadtime, the trigger electronics must itself be pipelined: every process in the trigger must be repeated in every 25 ns.

Thus, the aim is to maintain data flow synchronously with the repeated pattern of trigger logic which ends up with simple arithmetic operations or functions using memory lookup tables where an address of data produces a result previously written into the memory.

4.3 L1 Trigger System

We can summarize some of the main characteristics of the L1 Trigger System [32].

- ▶ The maximum input rate of the L1 trigger is 40 MHz bunch crossings compatible with the HCAL and ECAL trigger primitives computed out of the detector pulses. The digitization of the analog signals occurred at the same beam crossing rate.

- ▶ The output rate of the L1 trigger is in between 25 to 100 kHz, which is a bandwidth shared between muon and calorimeter triggers. Therefore it also specifies maximum rate that can be achieved by the High Level Triggers. This maximum trigger rate corresponds to a minimum rejection rate of 10^4 at design luminosity of $10^{34} \text{ cm}^{-2} \text{ s}^{-1}$

- ▶ All data is stored in a pipeline with $3.2 \mu s$ latency equivalent to 128 BX (25 ns Beam Crossings). During this period, trigger data must be collected from the front end electronics which implies that trigger algorithms cannot use full information available from the detectors.

- ▶ The trigger electronics are pipelined in order to avoid dead time. However a fraction smaller than %1 calculated dead time occur at L1 system can be considered as a good compromise.

- ▶ Since signal propagation delays are included in this pipelined time, The available time for L1 Trigger calculations is smaller then $\sim 1.5 \mu s$.

- ▶ In general, there are two detector systems which process L1 information. The first detector system is Muon Calorimeter Trigger further organized into DT(Drift Tube), CSC(Cathode Strip Chamber) and RPC (Resistive Plate Chamber).

The other detector system is the Calorimeter Trigger, which can be split into three parts as HCAL (Hadronic Calorimeter), ECAL (Electronic Calorimeter) and HF being the Forward Hadronic Calorimeter organized separately from HCAL.

- ▶ The L1 Detector system as a whole can be understood in 3 main steps: Local, Regional and Global.

► All input data into L1 Trigger system listed above transmitted to Data Acquisition System (DAQ) for storage along with the event readout data. However, the decision whether to trigger on a specific crossing or to reject that crossing is transmitted to front-end and readout systems via TTC (Trigger Timing and Control) system which also provides clock and control signal units.

► The TTC system in CMS is divided into a series of zones. Within each zone, signals can be broadcasted from a single laser source to more than a thousand destinations over a passive network composed of a hierarchy of optical tree couplers. Active optical/electrical converters (TTCrx) at each fiber destination provide programmable coarse and fine deskew to compensate for different particle flight times and detector, electronics, propagation and test generator delays. Prototype TTC hardware has been used successfully to provide clock and control signals in laboratory and beam tests by CMS.

► Copper cables are used in data flow between crates and they are useful in order to avoid the necessity for optical drivers with their cost, size and power requirements but have limited length capability.

► The key to a good trigger system is the flexibility. The CMS L1 trigger electronics has been designed to reach this purpose. Not only all thresholds are programmable, but as mentioned above, algorithms are either implemented in FPGAs or LUTs(Look Up Tables). Reprogramming the FPGAs or downloading new LUT contents allows for major revisions of the trigger algorithms.

The L1 Architecture can be illustrated with the Figure below 4.1

4.3.1 L1 Calorimeter Trigger

For a detail introduction on HCAL and ECAL, one can look at the previous chapter of this thesis. Considering Calorimeter Triggers containing HCAL and ECAL partitions located in the counting house USC55, one can generalize the overall procedure during the data process.

► In Local Calorimeter Trigger (LCT), the computation begins with the trigger tower energy sums formed by ECAL, HCAL and HF send to the TPG performing the first computation steps in the system and evaluate the calorimeter trigger primitives by transmitting the results to Regional Trigger System.

► In Regional Calorimeter Trigger, the physics constraints are applied such that candidates for electrons, photons, jets, isolated hadrons are found and transverse energy sums are evaluated. The E_T thresholds for each of these objects are required to be kept tunable so that

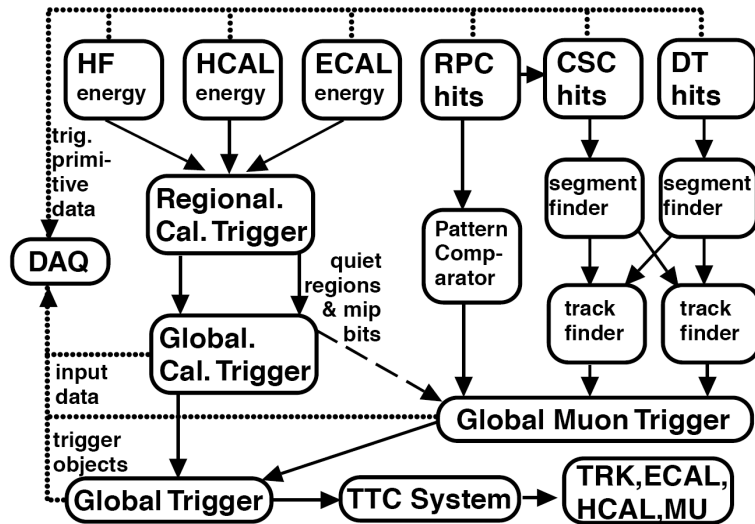


Figure 4.1: Overview of the Level 1 Trigger

the QCD background rates are tolerable and the efficiency for discovery physics is high, while providing sufficient sample of control events.

► In Global Calorimeter Trigger (GCT), All the physics object candidates are categorized together with the total and Missing Transverse Energy sums E_T . In order to improve the trigger efficiency of rare multi-jet events, a jet multiplicity trigger is also implemented alongside the main jet algorithms. The purpose of this final step is to reduce the amount of information as much as possible before sending it to GT (Global Trigger).

The Global L1 Trigger transmits a decision to either accept (L1A) or reject each bunch crossing. This decision is transmitted through the Trigger Throttle System (TTS) to the Timing Trigger and Control system (TTC). Besides handling physics triggers, the GT provides for test and calibration runs, not necessarily in phase with the machine, and for prescaled triggers, as this is an essential requirement for checking trigger efficiencies and recording samples of large cross section data.

4.4 High Level Trigger(HLT)

The CMS HLT is a purely software trigger run on the online computing farm. No additional intermediate trigger level is required after L1 stage, as the event builder is dimensioned such that complete events are directly assembled at the full Level-1 accept rate. The system must decide the fate of each event within a very short time in a challenging way without losing any significant event since the main requirement of the software trigger is to satisfy a diverse physics program with high efficiency [33].

The general strategy of the HLT implementation is based on using offline software as much as possible in order to keep the software robust and maintainable. Meaning that any event selection must be inclusive and must not require precise knowledge of calibration or run conditions since precision detector calibrations lag behind data collection. In order to do that, the event selection efficiency must be measurable from data alone so all algorithms and event processors must be monitored closely as events failing the online selection will be lost forever.

For that aim The CMS Filter Farm is integrated with the DAQ through a common framework capable of controlling, configuring, and monitoring the events in a reliable way. The internal architecture of each Filter Unit decouples the DAQ from the physics algorithms and provides the full-fledged offline reconstruction to process and filter detector events. Problematic events are handled without any impact on the operation of the global DAQ and recovered and stored for offline expert inspection.

The online selection code running in a single processor analyzes one event at a time and its job is to lower the L1 100 kHz rate to an output selection rate of 100 Hz, which is to say that it can accept only 0.1% of the processed events. The HLT has access to the full event data unlike the L1 trigger so it can make more demanding requests on the events. The main limitations of an online software trigger are that of available CPU time and the lack of precision of the calibration and alignment constants.

For the event signatures we considered in this study, HLT algorithms and performance issues of ME_T and Single Jet trigger paths will be discussed in Chapter 6.

CHAPTER 5

CMSSW : PHYSICS ANALYSIS IN CMS EXPERIMENT SOFTWARE ENVIREMENT

5.1 Reconstruction

In order to perform Physics Analysis, the information coming from different parts of the CMS detector should be combined by specifying track, vertex and higher level physics objects respectively. We can split this process mainly to 2 parts being the Reconstruction of Objects and the Reconstruction of Events based on [34].

5.1.1 Reconstruction of Objects

► TRACK RECONSTRUCTION

This process can be classified in 5 parts.

1. Hit Reconstruction obtains the position of the objects and estimates uncertainty of them by clustering the activated tracker pixels or strips.

2. Seed Generation is responsible for the definition of initial trajectories and error estimation by requesting at least 2 jets in the previous step.

3. Trajectory Building

For a charged particle in a magnetic field, the seed obtained from previous step is used to extrapolate the first suitable tracker layer. For each suitable hit, a trajectory candidate is created using Kalman filter formalism based on a Neural Network algorithm.

4. Ambiguity Resolution

Different seeds used initially, addressing the previous step, would correspond to more than 1 trajectory candidate. Thus one can prevent double counting of tracks in principle.

5. Final Track Fit, which completes the process by fitting the optimum track.

► VERTEX RECONSTRUCTION

It consists of finding and fitting the vertex by considering many different algorithms depending on the physics requirements.

► ENERGY RECONSTRUCTION

Considering energy deposits of ECAL and HCAL, the measurements made in both of these calorimeters are combined. Thus, calorimeter towers (ECAL + HCAL) are constructed by getting the signals in (η, ϕ) bins, which corresponds to a particular cell of HCAL. The efficiency depends on the success of the elimination of calorimeter noise together with the regular noise by applying an energy cut on all towers.

► STANDALONE MUON RECONSTRUCTION

Using the information coming from the muon system, this process can be decomposed into 3 steps. Then the information coming from different subdetectors (DT, CSC, RPC) are combined by building Kalman filter again.

1. Hit Position
2. Segment Reconstruction
3. Track Finding

5.1.2 Reconstruction of Events

► JET RECONSTRUCTION

A scattered parton associated to quark-gluon fragment is measured in the calorimeter being jets in which the particles produced are collimated in the direction of the initial parton due to the high boost. Thus, the easiest way to perform jet reconstruction consists of clustering the energy deposits in a cone, where the primary axis of the it coincides with the direction of the initial parton. Since Lorentz invariance is hold, these cone can be described in $\eta - \phi$ space, with the metric:

$$\Delta R = \sqrt{(\Delta\phi)^2 + (\Delta\eta)^2} \quad (5.1)$$

where η and ϕ represent the pseudorapidity and the azimuthal angle respectively.

A jet algorithm can be considered as a set of mathematical operations, which is responsible for reconstructing the properties of jets by combining transverse energies of their constituents. All the analysis in this thesis are performed with the PAT (Physics Analysis Tools), so a standard Cone Algorithm is considered with the following:

► ITERATIVE CONE ALGORITHM

1. Ordering the Input Objects: The algorithm is initialized by ordering the the input objects with respect to the transverse energy above a certain threshold defined as jet seed.

2. Constructing Proto-Jet: The objects remaining inside the solid angle of the cone are clustered in the direction of the jet seed. Thus, a proto jet being the replaced seed makes the iterations until the energy and the direction is stabilized.

3. Iterations by adding Proto-Jet: The final proto jet, which is obtained in the previous step is replaced with the ordered input objects and this process is repeated until the threshold value considered in the first place is reached.

The iterations mentioned here is made by using E_T scheme by dividing the jet transverse momentum to the sum of transverse energies. Then one can ends up with producing massless jets by fixing the direction of the jet with θ angle.

$$\sin\theta = \sum \frac{E_T}{E} \quad (5.2)$$

where E is the jet energy and E_T being the transverse energy. The reconstructed jets corresponding a particular 4-momentum and the fraction of the energy are deposited in the sub-partition of the calorimeter.

► MUON RECONSTRUCTION

Starting from the standalone reconstructed muon, the muon trajectory is extrapolated to the outertracker surface by regarding the muon energy loss in the crossed materials and the effects of multiple scattering. So the track reconstruction is done again with Kalman-filter technique and all the reconstructed tracks are refitted together with the standalone muon tracks.

► MISSING TRANSVERSE ENERGY RECONSTRUCTION

The large pseudorapidity coverage of the CMS detector allows for rather precise test of 2 dimensional momentum conservation in the plain perpendicular direction of the beams. It is clear that such a design aims to detect as much as possible final state possible so that the reconstruction of missing energy would be also possible. Thus, any measured significant imbalance in transverse momentum, Missing Transverse Energy (ME_T), can be considered as the signature of weakly interacting particles, which typically escape from the detector without being measured. ME_T in CMS is determined from the vector sum over uncorrected transverse energy deposits in projective Calorimeter Towers [35]. So the simplist way to reconstruct the

transverse energy is to calculate the negative vectorial sum over all energy deposits in the calorimeters.

$$\begin{aligned}
ME_T &= - \sum_n (E_n \sin\theta_n \cos\phi_n \hat{i} + E_n \sin\theta_n \sin\phi_n \hat{j}) \\
&= (ME_T)_x \hat{i} + (ME_T)_y \hat{j}
\end{aligned} \tag{5.3}$$

ME_T is a crucial observable for measuring not only the Standard Model (SM) processes but also for searching new physics beyond the SM, which are associated to relatively large magnitudes in general. Hence, establishing the nature of this important quantity is really complicated and requires careful studies to understand the detector and beam effects on it. One should be careful before claiming any discovery beyond SM because of this reasons. In this thesis ME_T is replaced by an MH_T quantity to eliminate various detector malfunctions and particles hitting poorly instrumented regions of the detector as explained in Chapter 6 extensively.

5.2 CMS Experiment Software

based on [36],[37],[38]

The whole collection of CMS Software is constructed around a framework called EDM(Event Data Model) which is used to access and store all event data. The purpose of this framework together with EDM is to facilitate the development and deployment of reconstruction and analysis software.

► EVENT DATA MODEL

An event is a container of many products, built by many different types of C++ programming language. All data format types and the content of events is designed around EDM in order to get a flexible event output utilized for the requirements of analysis. To store the information of the event data ROOT I/O is chosen since it is a forerunner technology considering the implementation of the event store and Reflex Dictionaries.

5.2.1 Event Data Tiers

CMS defines different data tiers, which are compatible for various applications such as alignment, calibration and physics analysis. Different data formats processed in Tiers are given below.

► RAW : contains the initial detector information used as an input for the high level filtering.

► RECO: composed of offline reconstructed objects.

► FEVT: Full Events contains RAW+RECO formats.

► AOD : is subset to the RECO format in which the physics analysis performed.

► GEN : is a format including generated Monte Carlo information.

► SIM : comprises the simulated energy depositions.

► DIGI: contains the simulated response of the electronic readout channels to the hits of the relevant detector elements.

5.2.2 PAT:Physics Analysis Toolkit

based on [39].

PAT is a high-level analysis layer providing the Physics Analysis Groups (PAGs) with easy access to the algorithms developed by Physics Objects Groups (POGs) in the framework of the CMSSW offline software. The main purpose is to fulfill the requirements of the most CMS analysis, providing both ease-of-use for beginners and flexibility for advanced users.

The production of PAT candidates starts from the AOD or RECO format. In order to associate trigger information, the PAT workflow is organized in a main sequence together with a parallel sequence. An outline for this sequence is given in figure 5.1

► aodReco

The main sequence starts from pre-production steps includes aodReco and mcMatching. The aodReco sequence adds useful information to the RECO candidates. For electron, muon, tau, and photon candidates, this includes:

1. The calculations of isolation variables using information from several detectors,
2. The association of isoDeposits to allow for more detailed studies,
3. The association of standard POG supported object identification variables.

For jet candidates, more information is implemented such as:

1. The association of charged tracks,
2. The corresponding jet-charge variable,
3. An association of jet energy corrections factors (to all potential levels of jet energy scale correction),
4. Algorithms for and information of (b-) flavour tagging,
5. The corresponding module definitions can be found in the recoLayer0 directory of the

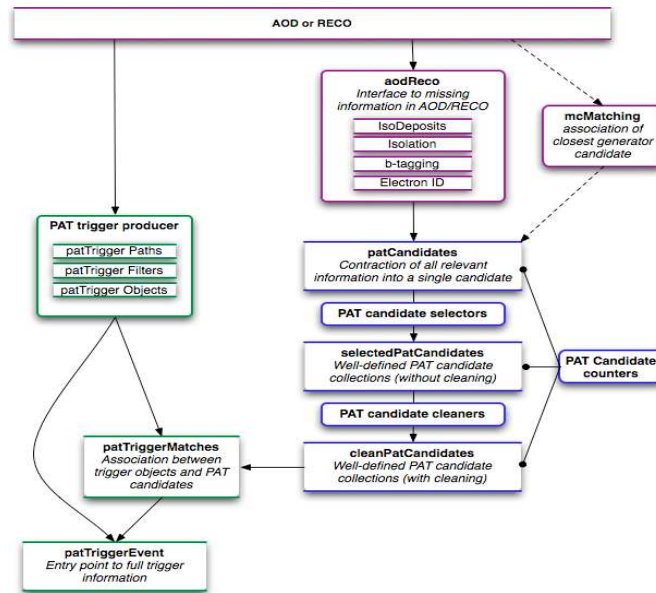


Figure 5.1: PAT Workflow

PatAlgos package.

Another important operation, `mcMatching`, which connects generator particles and the reconstructed candidates. The matching is an operation/selection based on the objects' similarity in their spatial and kinematical distributions.

► `patCandidates`

After the pre-production steps, the collections of `pat::Candidates` and `patCandidates`, which comprise of all relevant information are produced:

1. The corresponding module definitions can be found in the `producersLayer1` directory of the `PatAlgos` package.
2. They have the corresponding `reco::Candidates` and all relevant extra information (from AOD or RECO) as input.
3. All the needed extra information is collected via corresponding `cff` files in the same directory.

► `selectedPatCandidates`

The collections of `selectedPatCandidates` are produced after passing some potential selections in PAT candidate selectors. Note that the default selection criteria in this step are dummy selections, which effectively do not lead to a rejection of `pat::Candidates`. Though the user may add what ever object/event selection might be suitable for his analysis by replacing

the dummy selections in his configuration file.

1. The corresponding module definitions can be found in the `selectedLayer1` directory of the `PatAlgos` package.

2. They can have any collection of `pat::Candidates` as input. This can be `patCandidates`, `selectedPatCandidates` or `cleanPatCandidates`.

► **cleanPatCandidates**

Because of the organisation of the reconstruction software of CMS, some of the physics measurements might be doubly reconstructed as different physics candidates. For example, an electromagnetic cluster can be reconstructed as an electron, a photon and a jet would be presented in all the different collections at the same time. In a cleaning step, PAT provides an opportunity for adopting a cross-collections cleaning to remove some of the overlapping candidates, depending on the wish and configuration of the user. The remaining candidates are stored in `cleanPatCandidates` collections.

1. The corresponding module definitions can be found in the `cleaningLayer1` directory of the `PatAlgos` package.

2. They can have any collection of `pat::Candidates` as an input. This can be `patCandidates`, `selectedPatCandidates` or `cleanPatCandidates`.

► **PAT trigger event**

Besides the main PAT production sequence, trigger information is re-keyed into a human readable form in the `pat::TriggerEvent` and the PAT trigger matching provides the opportunity to connect PAT objects with the trigger objects. Thus, the user can easily figure out which object(s) fired the desired trigger bits. The production sequence starts from the PAT trigger producers, and folds the information in the `pat::TriggerObject`, `pat::TriggerFilter`, and `pat::TriggerPath` classes. These classes are finally contracted into the `pat::TriggerEvent` as a central entry point to all trigger information.

5.2.3 CSA07 Production

Regarding the 14 TeV Analysis in this thesis, all the background samples were picked by the Computing, Software and Analysis challenge performed in the Fall 2007 (CSA07).

The CSA07 production is targeted for $1 fb^{-1}$ of statistics and therefore the data samples have been reconstructed with calibration and alignment constants based on the understanding of the detector obtained with $100 fb^{-1}$ of data. Miscalibrations were not taken into account at the trigger level.

CHAPTER 6

ANALYSIS

6.1 Introduction

In this chapter, the analysis procedures for the monojet signature of ADD model within the LED (Large Extra Dimensions) context will be discussed. An approach, where extra spatial dimensions are compactified on a torus with common circumference R is imposed for the signal generation of ADD model. The selected events generated with $\sqrt{s} = 14$ TeV center-of-mass energy up to 100 pb^{-1} Integrated Luminosity will be compared with the $\sqrt{s} = 10$ TeV center-of-mass energy up to 200 pb^{-1} Integrated Luminosity. The Trigger studies performed for both of these analysis will be highlighted in detail and the cut based analysis will be summarized together with the discovery reach and exclusion limits, which are investigated as a function of M_D and δ in this section.

6.2 Direct Graviton Production Mechanism

In ADD model, the SM is confined on the ordinary Minkowski Space, called braneworld, while gravitons considered as a massless spin-2 particles are free to roam through the $4 + \delta$ dimensioned space. At an energy scale corresponding to the TeV energies within the reach of LHC, this process would be projected onto the ordinary 3 spatial dimensions, where the SM lives, and appear as a tower of light Kaluza-Klein excitations. Gravitons are weakly coupled to the ordinary matter, so they escape from detection but would be inferred from the amount of missing energy.

In this analysis, we focused on the production of a graviton G balanced by an energetic hadronic jet via the processes $q\bar{q} \rightarrow gG$, $gg \rightarrow gG$, $qq \rightarrow qG$, which are illustrated in figure 6.1

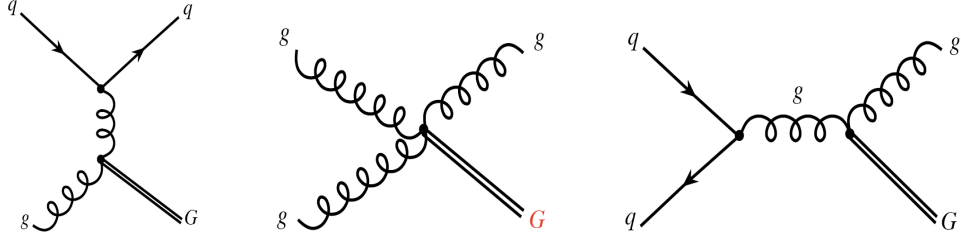


Figure 6.1: Different production modes for the Direct Graviton channel within ADD Framework

The differential cross sections with a graviton of mass m for the parton processes, which are relevant to $G + \text{Jet}$ production in hadron collisions are given below.

$$\begin{aligned}
 \frac{d\sigma_m}{dt}(q\bar{q} \rightarrow gG) &= \frac{\alpha_s}{36} \frac{1}{sM_{Pl}^2} F_1(t/s, m^2/s) \\
 \frac{d\sigma_m}{dt}(qg \rightarrow qG) &= \frac{\alpha_s}{96} \frac{1}{sM_{Pl}^2} F_2(t/s, m^2/s) \\
 \frac{d\sigma_m}{dt}(gg \rightarrow gG) &= \frac{3\alpha_s}{16} \frac{1}{sM_{Pl}^2} F_3(t/s, m^2/s)
 \end{aligned} \tag{6.1}$$

Here F is a usual flux factor for the collision of two particle where t is the Mandelstam variable defined as $(p_q - p_G)^2$. Since the graviton interaction vertex is suppressed by M_{Pl}^{-1} , it can be anticipated that $\sigma_m \propto \bar{M}_{Pl}^{-2}$.

Then the inclusive cross section for the production of graviton in partonic interactions with the energy scale $\sqrt{\hat{s}}$ (center-of-mass energy) can be written in terms of the fundamental scale M_D and the number of extra dimensions δ [40].

$$\sigma \approx \frac{1}{M_D^2} \left(\frac{\sqrt{\hat{s}}}{M_D} \right)^\delta \tag{6.2}$$

6.3 Current Limits

Regarding $\gamma + ME_T$ and $\text{Jet} + ME_T$ final states, searches performed by LEP [41],[42], $D\phi$ [43][44] and CDF have been showed that there is no deviation from SM expectations with the %95 Confidence Level (CL) up to now. The current limits are given in table 6.1 where the lower limits on M_D for several number of extra dimensions are reported [45]. Depending on the variations of the number of extra dimensions, it can be seen that Tevatron experiments have a better resolution than LEP experiments.

Table 6.1: For the $\gamma + ME_T$ and Jet + ME_T signatures with 95% Confidence Limits specified by different experiments in TeV order

δ	LEP	D ϕ		CDF		
	$\gamma + ME_T$	Jet + ME_T (1.1 fb^{-1})	$\gamma + ME_T$ (2.0 fb^{-1})	Jet + ME_T (1.05 fb^{-1})	$\gamma + ME_T$ (78.8 fb^{-1})	combined
2	1.600	0.99	0.921	1.310	1.080	1.400
3	1.200	0.80	0.877	1.080	1.000	1.150
4	0.940	0.73	0.848	0.980	0.970	1.040
5	0.770	0.66	0.821	0.910	0.930	0.980
6	0.660	0.65	0.810	0.880	0.900	0.940

When it comes to LHC, Table 6.2 shows the sensitivity of ATLAS [46] and CMS experiments with respect to the different luminosity conditions. As it can be seen in this table, using the same data size, current exclusion limits of ADD can be significantly improved for 10 TeV case. The current limits of the CMS experiment has been put with the analysis [47],[48] for 14 TeV and 10 TeV cases discussed in this thesis. Considering indirect searches, the results

Table 6.2: For the Jet + ME_T signatures with 95% Confidence Limits expected at LHC in TeV order

δ	ATLAS		CMS	
	(30 fb^{-1})	(100 fb^{-1})	(100 pb^{-1})	(200 pb^{-1})
2	7.7	9.1	4.61	3.1
3	6.2	7.0		
4	5.2	6.0	3.46	2.3

coming from Newtonian Potential measurements showed $R < 190 \mu m$ as a limit for the $\delta = 2$ case, where the value of M_D depends on a compactification mechanism given in [49]. Astrophysical results given on the observations of SN1987A Supernovae, graviton emission has led to a lower limit $M_D=1.6$ TeV for $\delta = 3$ despite the huge amount of uncertainties coming from the lack of knowledge on the temperatures of the inner core of the system [50].

6.4 Monte Carlo Generation of Signal and Background Samples and Reconstruction

Our signal constitutes a high-transverse-momentum Jet in the central region of the detector ($|\eta| < 1.7$), accompanied by possible less energetic jets due to the initial-final state gluon

radiation. The key issue about the MonoJet signature is that there would be no other energetic jets produced neither central nor in the forward direction. For the case of 14 TeV analysis the high p_T selection is for $p_T > 400$ GeV, where in 10 TeV case, this selection is reduced to $p_T > 200$ GeV since the jet magnitude is recoiling back-to-back in the transverse plane with the ME_T as a constraint on the prior selection criteria.

The new physics signature considered in this study would be suppressed by several SM processes. The most relevant ones regarded as background are :

► **Z+JETS** with the Z decaying into two neutrinos forms ‘irreducible’ background: This channel leads to invisible energy recoiling against jets and is described by the same signature as the signal. The contribution from this irreducible background needs to be estimated in the best possible way to be subtracted.

► **W+JETS** When the charged lepton (e, μ, τ) is not reconstructed by the detector, the signal is faking and turns out to be similar to the Z+jets one with a leptonic W decay;

► **QCD DI-JETS**. A possible mismeasurement on a single or multiple jet magnitude would stem from the contribution of this known background. Moreover a significant amount of ME_T would be produced in Hadron decays, mostly dominated by the high p_T neutrinos and high p_T particles outside the detector acceptance.

► **TOP QUARK PRODUCTION**

Both Top pair and Single Top Quark Production can mimic the signal for events with few or collimated jets when missing energy and energetic jets point in opposite directions. However events where leptons are not identified may also lead such variations in this case.

► **ZZ/WW/ZW + JETS** processes have also minor contribution to the data set because of low cross section however they would correspond to a large ME_T in some cases.

MACHINE INDUCED BACKGROUND

Referring the various detector malfunctions act on the ME_T quantity mentioned in Chapter 5, the dominant effects would comprise of 3 distinct categories in general:

► INSTRUMENTAL EFFECTS: DEAD/HOT TOWERS, PU (PILE UP)

The systematic uncertainties due to the noisy and dead channels in the hadronic and electromagnetic calorimeter effects the determination of the physics objects and would result an undetermined amount of ME_T .

While this high luminosity is essential for many searches of rare new physics processes at high energy scales, it also complicates analyses, because at each bunch crossing there will be of the order of 20 minimum bias pp interactions, which pollute any interesting hard events with many soft particles. The beams at LHC will have a longitudinal spread, and it may be possible experimentally to associate each charged particle with a distinct primary vertex that corresponds to a single pp interaction and so eliminate some fraction of the soft contamination. However, for neutral particles this is not possible, and most jet measurements are in any case expected to be carried out with calorimeters, which do not have the angular resolution needed to reconstruct the original primary vertex. Therefore kinematic measurements for jets will be adversely affected by pileup (PU), with resolution and absolute energy measurements suffering significantly [51].

From Tevatron studies, being replaced by ME_T vector, MH_T quantity is expected to be less affected by instrumental effects like pile up and detector noise (HPD Noise, Presshower Si sensors, APD's, MSGC and etc.) [52]. Here the mentioned instrumental background is slightly stimulated by the QCD events tried to be reduced as a main goal in Trigger studies.

► COSMICS AND BEAM HALOS

Beam halo particles arise from the interaction the of beam with residual gases within the LHC vacuum pipe. The charged particles that stem from this occurrence can have their trajectory affected by the magnetic field of the devices, commonly known as magnets, that are used to focus the beam. Beam halo particles mainly consist of hadrons which decay to muons. Since these particles come from such a highly energetic source, the energy that they can obtain is significant. Halo particles can travel through the CMS detector and deposit energy via bremsstrahlung, a process in which the muon radiates electromagnetic radiation by releasing a photon due to interacting with metal [53]. This can cause a discrepancy in energy conservation during a physics collision, resulting in large amounts of missing transverse energy ME_T .

Cosmic ray contribution will also be important because they pass through detector components that are otherwise unconnected by tracks would end up with considerable amount of ME_T .

► NONLINEAR CALORIMETER RESPONSE

There are also effects of Jet Energy Fluctuations on the calorimeter which causes non linear calorimeter response both in hadronic and electronic subparts of the CMS. Since the systematic differences in the average calorimeter response are integral part of the energy resolution, it is hard to discriminate the signal topology in many cases.

6.4.1 Signal Generation

The ADD Signal are produced with the SHERPA Monte Carlo generator, version 1.0.11 for 14 TeV and 1.1.2 for 10 TeV analysis [54]. In order to obtain a good resolution in a large parameter space, samples at various M_D fundamental scale with different number of δ are generated for both center-of-mass cases and full detector simulation is also applied [55].

Since the ADD cross sections are usually computed in an effective theory approach [40], the cut prescription $\sqrt{\hat{s}} < M_D$ has been directly applied in the generation step where $\sqrt{\hat{s}}$ is the center of mass energy of the partonic interaction. A \hat{p}_T cut-off on the parton recoiling against the graviton is also introduced by requiring $\hat{p}_T > 200$ GeV condition using the CTEQ61L Parton Density Functions (PDF) [56]. Here \hat{p}_T is intended as the transverse momentum of the outgoing parton in jet production (gluon or quark) The table 6.3 is for 10^5 events per subsample for the generation parameters given above. The p_T distribution of generated

Table 6.3: ADD cross sections (and errors from generation stage) as evaluated by the SHERPA program for $\sqrt{s} = 14$ TeV where all values are in terms of pb.

	$\delta = 2$	$\delta = 3$	$\delta = 4$
$M_D = 2$ TeV	49.246 ± 0.056	29.147 ± 0.033	18.914 ± 0.022
$M_D = 3$ TeV	12.462 ± 0.015	6.392 ± 0.007	3.874 ± 0.005
$M_D = 4$ TeV	4.253 ± 0.005	1.844 ± 0.002	0.998 ± 0.001
$M_D = 5$ TeV	1.783 ± 0.002	0.650 ± 0.001	0.308 ± 0.001
$M_D = 6$ TeV	0.862 ± 0.001	0.266 ± 0.001	0.109 ± 0.001
$M_D = 7$ TeV	0.466 ± 0.001	0.124 ± 0.001	0.044 ± 0.001

graviton and the $\Delta\phi$ (leading jet, ME_T) with respect to the number of events is given in figure 6.2 [47]. By looking at the graviton transverse momentum on the left, it can be seen that the jet multiplicity and the event shape do not show any striking dependence on δ , thus a larger M_D will only result with a more energetic graviton.

For the $\sqrt{s}=10\text{TeV}$ case, each subsample for a specific benchmark point (M_D, δ) is generated with the signal cross sections at leading-order. By reducing the value of M_D , we deal with relatively large cross sections where \hat{p}_T cut is also reduced to 150 GeV. Cross sections with negligible errors for $2 \cdot 10^4$ events per subsample is given on table 6.4.

Table 6.4: ADD cross sections (and errors from generation stage) as evaluated by the SHERPA program for $\sqrt{s} = 10$ TeV for all values in terms of pb.

	$\delta = 2$	$\delta = 3$	$\delta = 4$	$\delta = 5$	$\delta = 6$
$M_D = 1$ TeV	279.11	171.79	109.98	70.50	44.45
$M_D = 2$ TeV	33.03	17.41	10.64	6.92	4.58
$M_D = 3$ TeV	7.28	3.02	1.57	0.93	0.58

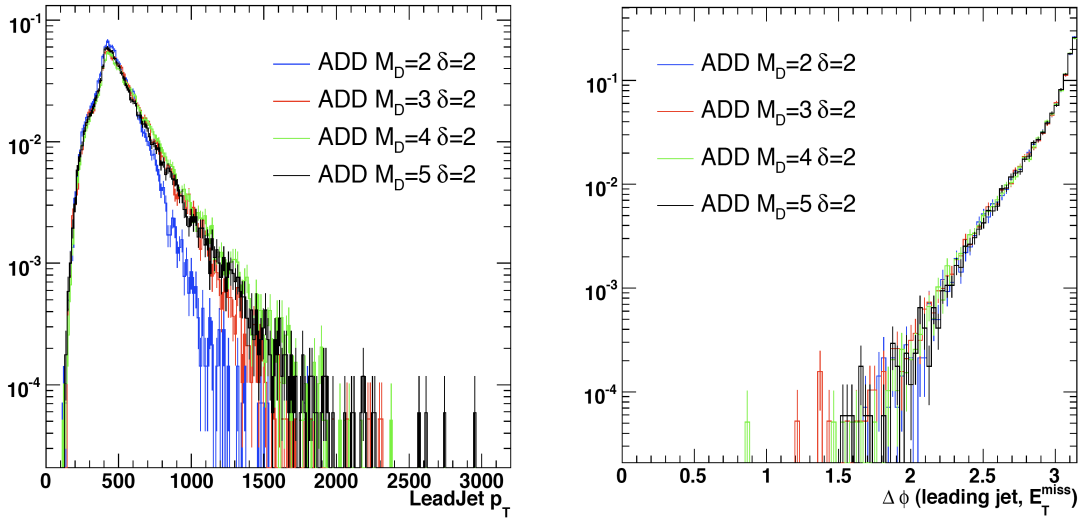


Figure 6.2: The p_T of generated graviton (left) and the azimuthal angular difference between the leading jet and the missing transverse energy (right) at generator level, for various benchmark points. No significant discrepancies between the different ADD signals have been found.

In order to evaluate the probabilities in which a certain event would occur, counting method is used to distinguish the number of parameters giving rise to similar processes. Thus the fundamental principle of counting is applied when many selections are made from the same set of objects while the order of selections do not matter in general. Hence, once SM background has been modeled properly, the $ME_T + 1$ Jet channel is expected to manifest itself as an excess on the ME_T spectrum on top of the background samples after specifying the control regions, where SM background would suppress the signal.

6.4.2 Background Generation

The hadronization of quarks and gluons (along with the underlying events) were performed using PYTHIA with the MLM shower matching prescription [57] to ensure that there is no double counting due to the parton showering in PYTHIA.

The Background processes considered here have been generated with a sample size corresponding to an integrated luminosity of 100 pb^{-1} and 200 pb^{-1} for 14 TeV and 10 TeV cases respectively. Details on the generated events per process are given in table 6.5 and table 6.6, along with the cross sections scaled with the branching ratios and the corresponding integrated luminosity. When a binning in p_T has been used, the number of events is integrated over the full range.

Table 6.5: Overview of the Background Statistics produced in the CSA07 for 14 TeV Analysis where (*) stands for the k-factor

SM Channel	Notes	$\sigma \cdot \text{BR}(\text{pb})$	Gen. Events ($\times 10^3$)
Z+jets	$0 < \hat{p}_T < 3200 \text{ GeV}$, inclusive sample	2792	567.5
Z ($\rightarrow \nu\nu$) + Jets	$0 < \hat{p}_T < 3200 \text{ GeV}$	239.1	265.1
QCD di-jets PDJetMet	extracted from Gumbo	2.531×10^6	6322
QCD di-jets PDMuon	extracted from Gumbo	2.531×10^6	152.6
W ($\rightarrow e\nu$) + Jets	$0 < \hat{p}_T < 3200 \text{ GeV}$	14.767	579.1
W ($\rightarrow \mu\nu$) + Jets	$0 < \hat{p}_T < 3200 \text{ GeV}$	14.767	579.1
W ($\rightarrow \tau\nu$) + Jets	$0 < \hat{p}_T < 3200 \text{ GeV}$	14.767	579.1
$t\bar{t}$	extracted from Chowder	$447 \times 1.85^{(*)}$	19,696
single-t (incl. e)	inclusive e channel	27	52.81
single-t (incl. μ)	inclusive μ channel	27	48.24

Table 6.6: Overview of the Background Statistics for 10 TeV Analysis

SM Channel	Notes	$\sigma \cdot \text{BR}(\text{pb})$	G.Evts ($\times 10^3$)	Int.Lum(pb^{-1})
Z ($\rightarrow \nu\nu$) + Jets	Sum08, MADGRAPH FullSim	3700	10^3	270
QCD $\hat{p}_T > 80 \text{ GeV}$	Sum08, PYTHIA FullSim	1,934,639	3×10^3	1.5
QCD $\hat{p}_T > 170 \text{ GeV}$	Sum08, PYTHIA FullSim		$62,563 \times 10^3$	48
QCD $\hat{p}_T > 300 \text{ GeV}$	Sum08, PYTHIA FullSim	3665	3×10^3	820
QCD $\hat{p}_T > 470 \text{ GeV}$	Sum08, PYTHIA FullSim	316	3×10^3	9500
W ($\rightarrow \lambda\nu$) + Jets	Sum08, MADGRAPH FullSim	35,550	10^4	281
$t\bar{t}$	Fall08, MADGRAPH FullSim	317	10^3	3150
single-t(tW, s-ch,t-ch)	Sum08, MC@NLO FullSim	93	550	5910

Regarding the 14 TeV case, most part of the background samples are selected by the

CSA07 soup mentioned in Chapter 5 of this thesis. Considering the generation, the CMS SoftWare version 1.4.6 [58] is used and CMSSW 1.6.7 is used for the reconstruction processes.

The so-called ‘Gumbo’ part of CSA07 inclusive sample ‘soup’ was used for non-diffractive di-jet production and minimum-bias background events. The inclusive $t\bar{t}$ production is sorted among the ‘Chowder’ component of the soup.

For both of the analysis compared here, reconstruction and the analysis step have been entirely performed using the Physics Analysis Toolkit (PAT), which applies standard energy corrections to the jets and computes isolation parameters for the leptons inside CMSSW framework [59]. Jets are obtained using an iterative cone (IC) algorithm with a fixed cone radius of $\Delta R=0.5$ [60] in $\eta - \phi$ space, where ϕ represents azimuthal angle. The results do not depend significantly on the clusterization details and the jet energy scale is corrected by applying a MC based energy correction. This includes the relative corrections by producing uniform response along η direction and the process ends up with correcting the jet energy back to the generator particle level [61].

6.5 Trigger Selections

6.5.1 Trigger Selection and Optimization for 14 TeV Analysis

Since a detailed introduction to the Trigger System is already given in the Chapter 4, the main task in this subsection is to apply the physics constraints compatible with the monojet channel in order to look for high momentum jets and/or large amounts of missing energy ME_T at the first level trigger (L1) and higher level filtering (HLT). Among the different trigger paths available in CMSSW, the ones that would be considered for new physics trigger at 14 TeV are given below.

- ▶ *Simple Single Jet Streams*, selecting one jet at L1 exceeding a p_T threshold (70-110-180-250 GeV thresholds are available in CMSSW);
- ▶ *Simple High Missing Energy Trigger* selecting $ME_T > 50$ GeV at L1 and $ME_T > 75$ GeV at the High Level Trigger (HLT);
- ▶ *Combined Triggers* filtering the single jet at L1 (p_T (jet) > 150 GeV) then add higher energy at HLT ($ME_T > 75$ GeV, p_T (jet) > 180 GeV).

In order to get a significant clean up related to the systematical uncertainties expected at the early phase of LHC, ME_T vector is avoided to be used directly and the common variables (E_T, ME_T) are intended to be replaced by another pair (H_T, MH_T) for 14 TeV trigger study.

6.5.2 Implementation of H_T and MH_T quantities

At L1, All the quantities inspected under the Machine Induced Background are calculated in the Global Calorimeter Trigger (GCT) of CMS detector and contribute directly to the ME_T distribution.

Nevertheless, an alternative solution can be proposed if the sum of moduli of transverse momenta $p_T(j)$ of all jets above a certain threshold p_T^0 can be introduced to specify H_T parameter, which stands for the scalar sum of the transverse energies in an event.

$$H_T = \sum_{p_T(j) > p_T^0} |\vec{p}_T(j)| \quad (6.3)$$

By doing that, the hadronic activity takes over the distribution to discriminate the physical processes like decays of massive particles. Moreover, determining H_T is less time consuming than E_T in the trigger farm so HT-based triggers are preferred for many analysis.

Thus, ME_T vector, which encounters the vector sum of the calorimeter cells, can be replaced by MH_T , which is built from the reconstructed E_T of jets accumulated from Jet candidates within the range $\eta < 5$. Thus, the moduli of the vectorial sum of jets transverse momenta above a certain threshold p_T^0 can be defined as MH_T parameter.

$$MH_T = \left| \sum_{p_T(j) > p_T^0} \vec{E}_T(j) \right| \quad (6.4)$$

The comparison between H_T and E_T together with MH_T and ME_T with respect to the QCD response is correlated in the figure 6.3

A large fraction of QCD events have small H_T and MH_T , thus an early selection relying on these quantities could be effective in improving the signal purity. The key issue is that the (ME_T) is calculated from a vector sum of calorimetric towers' transverse energies so it could be distorted by instrumental effects (dead/hot towers, beam halo, cosmic rays) together with pile-up and UE contributions. On the other hand, MH_T has a direct access to jets by definition and expected to be less affected from detector noise and pile-up events.

The E_T triggers in general use the transverse energy sums (electromagnetic + hadronic) computed in calorimeter regions (4x4 trigger towers in barrel and endcap). E_x and E_y are computed from E_T using the coordinates of the calorimeter region center [32] as depicted in figure 6.4 By replacing E_T with H_T , MH_T parameter is calculated by cropping the energy

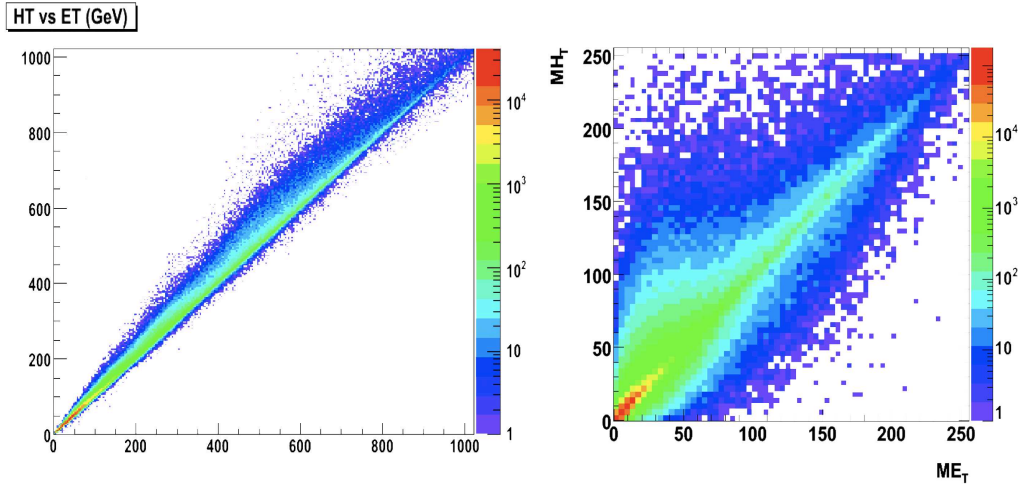


Figure 6.3: Correspondence of (H_T, E_T) pair to (MH_T, ME_T) without applying any cut on a Low mass QCD Sample

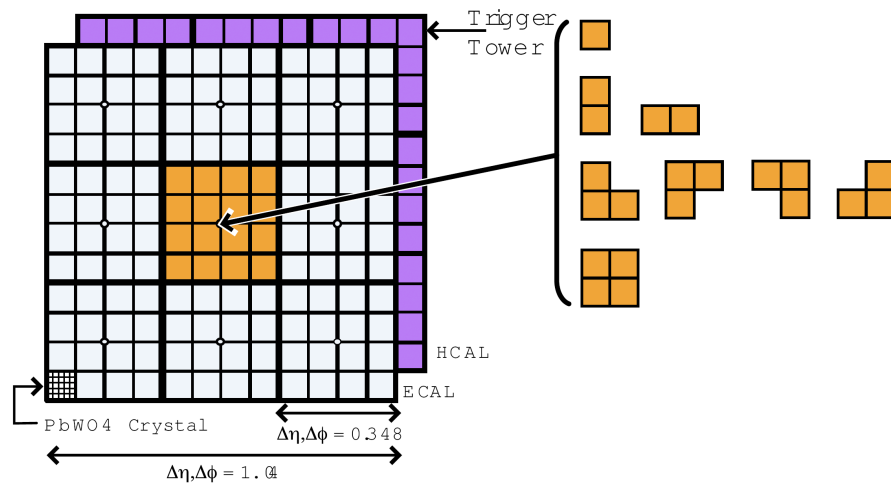


Figure 6.4: Jet trigger algorithm

sums and defined by a threshold value just like a ME_T vector. At L1, The global trigger accepts the definition in parallel, and apply the conditions for different selections of MH_T cuts. As a result H_T+MH_T trigger can be implemented with a number of thresholds used as a combination in order to control the physics objects recognized by the towers. This process prohibits the use of iterative algorithms, such as jet-finding, which is based on finding a seed tower. Then adding the surrounding towers make the jet energy sum.

The trigger stream proposed by SUperSYmmetry (SUSY) group is exploited in this analysis in order to benefit the large bandwidth stems from the di-jet background giving rise to large amount of ME_T and high p_T jets. Despite a quite richer final state, SUSY studies on jets have to deal with a kind of background fairly similar to the ADD Analysis at 14 TeV. Therefore such a 2 layer H_T+MH_T trigger is found to be the compatible with the early stage analyses of this study.

To summarize the procedure, an event will be fired by H_T+MH_T trigger if it satisfies all the conditions specific to each trigger level. The Level 1 condition requires trigger towers with a threshold value above $H_T > 200$ GeV with a $p_T^0 > 10$ GeV threshold. At an integrated luminosity of 100 pb^{-1} , it corresponds to a rate approximately 2.2×10^4 Hz at this stage. After then, at HLT level, a simultaneous cut is applied on H_T via increasing the jet threshold to 20 GeV followed by an MH_T cut. Thus MH_T parameter is computed out of the offline jets with $H_T > 250$ GeV and reconstructed with 4×4 trigger towers. The concurrent cut on $MH_T > 100$ GeV reduces the QCD rate as much as ~ 3.2 Hz as illustrated in the figure 6.5 proposed in [62]. Figures 6.6, 6.7 illustrate how signal efficiency varies with the changes of the

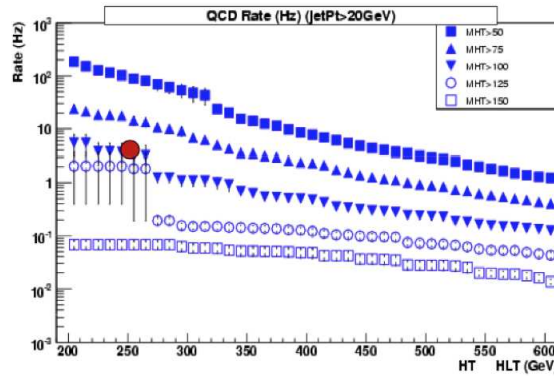


Figure 6.5: QCD Rate with the projection of Jet p_T^0 threshold for H_T+MH_T Trigger

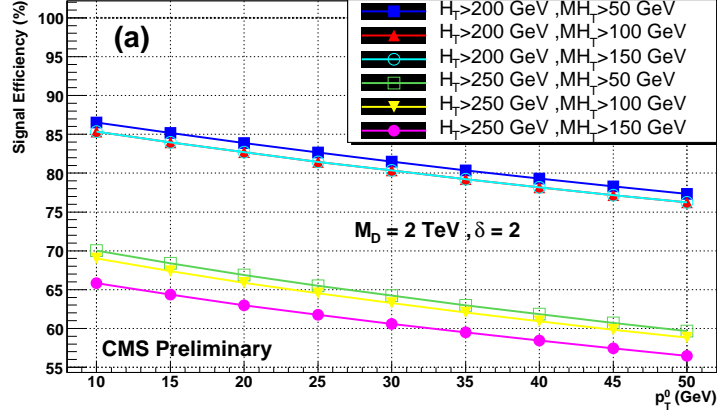


Figure 6.6: H_T+MH_T Trigger efficiency for $M_D=2, \delta=2$ benchmark point as a function of p_T^0 threshold for different selections.

Table 6.7: Summary of the cuts applied by H_T+MH_T Trigger

	H_T (GeV)	MH_T (GeV)	p_T^0 (GeV)	QCD Rate (Hz)
Level 1	>200		>10	2.2e+4
HLT	>250	>100	>20	3.2

isolation and matching cuts given in the table 6.7

The left hand plot of figure 6.8 shows the efficiencies before H_T cut is applied and on the right, the variations of different benchmark points of ADD signal after applying $MH_T > 100$ cut is showed. Note that the p_T cut at HLT level is raised to 25 GeV for this pair in order to show the flexibility of the jet transverse momentum with respect to the signal selection since variations of these cuts do not make major changes on this selection criteria.

6.5.3 Trigger Selection for 10 TeV Analysis

After the reviews on 2009 Triggers at TSG (Trigger Studies Group), It was obvious that the triggers working well for the generic objects would not respond to the specific assumptions on exotic channels because of the major systematic effects expected at start-up conditions. Considering the difficulties with the validation of combined and prescaled triggers with online analysis, the most basic selections are suggested in order to minimize the risk of any bad behaviour on the signal. Thus, 1E31 Trigger table ($10^{31} \text{ cm}^{-2} \text{ s}^{-1}$ Luminosity) is revised [63] and a more reliable and robust trigger is decided to be used following the beam energy reduction and the lowered p_T cuts. Then the selections of thresholds do not result from

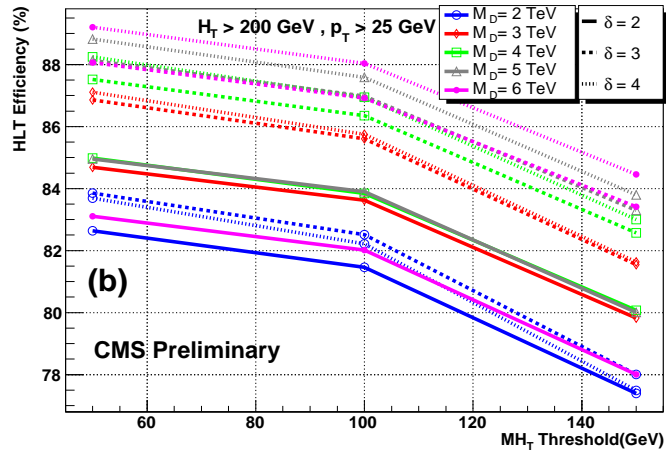


Figure 6.7: After $H_T > 200$ GeV, $p_T > 10$ GeV cut is applied, HLT efficiency as a function of MH_T threshold is given for different benchmark points of ADD Signal

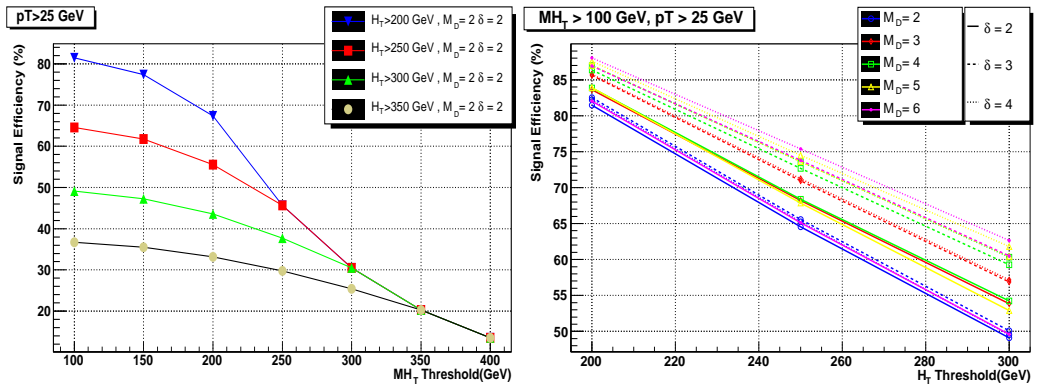


Figure 6.8: On the left, the efficiencies before H_T cut is used and on the right efficiencies of different benchmark points of ADD signal after $MH_T > 100$ GeV cut applied.

a sophisticated significance maximization, but they are determined by looking for a high $N_S/\sqrt{N_B}$ ratio (significance), where the (N_S, N_B) represents number of signal and background events respectively.

Among the ME_T and Jet triggers within 1E31 Trigger table together with ME_T triggers of 8E29 table, the ones which are compatible with our signal for 10 TeV case can be summarized with the table 6.8. A detailed table on the result of trigger paths can be found in

Table 6.8: Possible Trigger paths concerned for ADD Monojet at 10 TeV Study

HLT path	L1 Seeds	L1 pres.	HLT pres.	Type	Lum ($cm^{-2} s^{-1}$)
(ME_T Triggers)					
HLT_HT300_MHT100	L1HTT200	1	1	Physics	10^{31}
HLT_MET50	L1_ETM40	1	1	Physics	10^{31}
HLT_MET35	L1_ETM30	1	1	Physics	8.10^{29}
(Jet Triggers)					
HLT_Jet110	L1_SingleJet70	1	1	Physics	10^{31}

appendix A, before and after the selections are applied.

Concerning the 10 TeV case, MH_T parameter is implemented to the analysis in the prior selections and since the low statistic issue turns out to be compelling at the early phase of the LHC, it is found reasonable to abandon the H_T - MH_T trigger path, which results a large phase space giving enough room to tune subsequent thresholds.

Thus the jet stream, designed for a phase with $10^{31} cm^{-2} s^{-1}$ requiring at least one jet with $p_T > 70$ GeV at Level 1 (L1) and at least one jet with $p_T > 110$ GeV at HLT is chosen. This trigger path is not prescaled and selects $\sim 100\%$ of the samples with low p_T cut on the parton density of 150 GeV. Moreover, even if HLT rate seem to raise a bit high compared to the alternative paths, it is feasible for monitoring issues. In below prescription, the most important aspects of trigger selection at 10 TeV is given.

► The jet energies are evaluated using corrected jets. Both the L1 and HLT triggers are intended to be unprescaled throughout the duration of the initial CMS run so the multi-jet event rate at HLT level is predicted as 8.1 ± 1.1 Hz.

► The High Level Trigger response was reproduced with reconstructed offline jets. The efficiency of this trigger path is given in the figure 6.9 as a function of the MH_T lower cut. As shown in the following, these variables are demonstrated to be very effective in enriching

the signal events as well as the events with $MH_T > 250\text{GeV}$ where the cumulative efficiency of the signal reaches close to 100 %

► The effect of a harder cut on HLT threshold is also explored by rising the p_T cut to 180 GeV. Reduction on the acceptance of the background (about 80%) is larger than the signal ($\sim 40\%$) but this gain is compensated by a much less effectiveness of the off-line selections. Hence, HLT_Jet110 path is considered the optimal choice at 10 TeV studies.

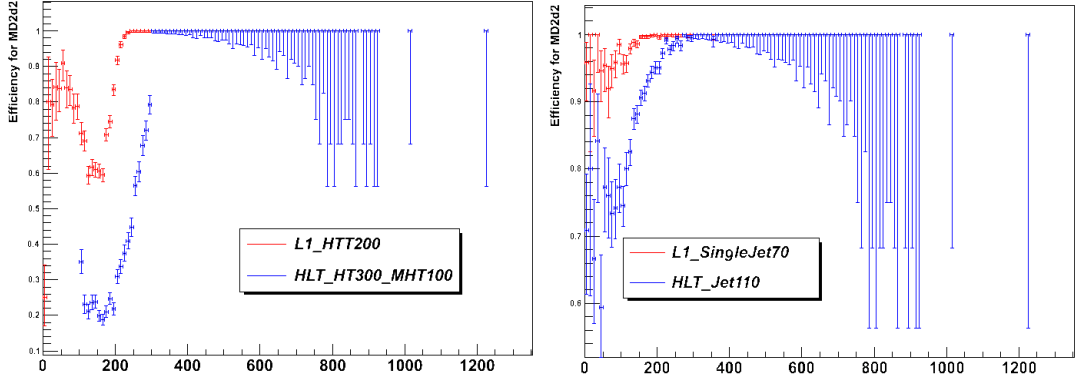


Figure 6.9: Comparison for the Efficiencies of the H_T+MH_T Trigger and Single-Jet trigger corresponding to the ADD signal with $M_D=2$ TeV and $\delta=2$ projected on MH_T

6.6 Signal and Background Analysis and Selections

In this section, the cut based analysis procedures in standard reconstruction algorithms provided by PAT is used. The obtained PAT objects including jets, muons and photons are used to make the signal and background estimation while calculating the missing transverse energy vector.

The threshold cuts on these PAT objects, which have been demonstrated to be capable of reducing the SM backgrounds, have been optimized with the purpose of maximizing the significance in the relevant kinematic region.

For the identification of Jets, an iterative cone (IC) algorithm with $\Delta R = 0.5$ is used, but the results quoted here doesn't necessarily depend on the clusterization details. Since the cleaning of jets from electrons is performed with off-line analysis, no electron-jet separation is applied in reconstruction of jet objects. We can divide the cut based analysis procedure into 4 sequential steps:

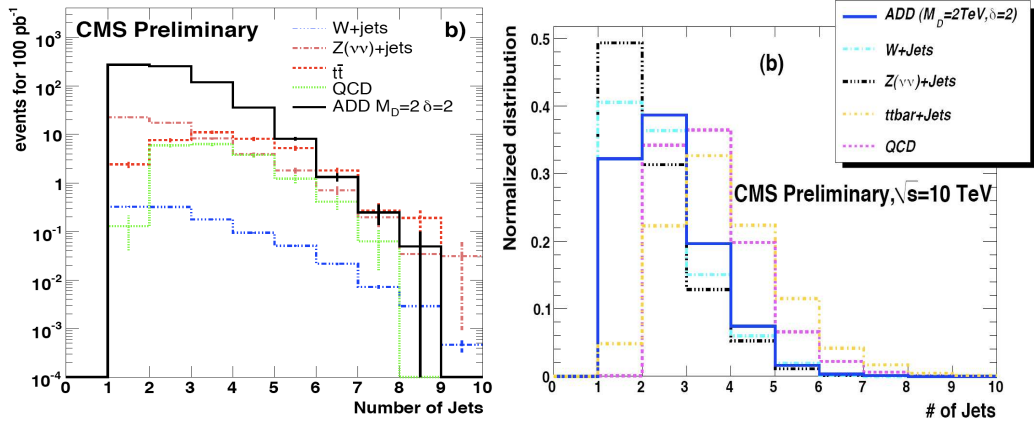


Figure 6.10: Number of jets for signal and relevant backgrounds, for $ME_T > 400$ GeV and jets with transverse momenta larger than 40 GeV at $|\eta| < 3$ for 14 TeV case. A veto against three or more Jet events turns out to be the optimal cut for minimizing the QCD contribution at 10 TeV analysis requiring $MH_T > 250$ GeV with $p_T > 50$ GeV selections. Histograms are overlaid and normalized to the same area.

- I. Requirements at the Preselection Level
- II. Charged Leptons Cleaning Cuts
- III. Kinematic Cuts and QCD Reduction
- IV. Imposed Topological Constraints

6.6.1 I. Requirements at the Preselection Level

In order to reduce the impact of hard gluon radiation in the selection, the 14 TeV analysis exploited a collection of signal and background samples having jets with $p_T > 40$ GeV transverse momenta and $|\eta| < 3$. For 10 TeV analysis p_T cut is raised to the 50 GeV in order to encounter the increased integrated luminosity.

At the early pre-selection level, $ME_T > 400$ GeV cut is imposed at 14 TeV case while it is reduced and replaced with the $MH_T > 250$ GeV at 10 TeV case. In order to reduce the impact of objects not coming from hard interaction, only jets with transverse momenta larger than 50 GeV within the hadronic calorimeter acceptance $|\eta| < 3$ are considered. These simple cuts have a significant role in eliminating multi-jet background, for which the events have typically few jets balanced in transverse energy, possibly accompanied by softer jets.

6.6.2 II. Charged Leptons Cleaning Cuts

Before doing further selections on jet objects, it is important to clean the events from contaminations with isolated leptons (as those from the $W(l\nu)+\text{jets}$ channel), electrons and photons identified as jets. Then the data sample would be cleaned from leptonic events by using the *Indirect Lepton Veto* approach, which requires the definition of two additional variables namely JEMF and TIV [64].

► **JEMF (JET ELECTROMAGNETIC FRACTION)** is defined as the fraction of the jet energy collected by ECAL over the total energy in hadronic and electromagnetic calorimeters. High energy electrons and photons are rejected by the requirement in which JEMF is lower than 0.9 value, since electrons and photons clustered as jets are characterized by JEMF of 1. The instrumental background, which may lead to fake jets, can also be reduced with the cut $JEMF > 0.1$. Thus, when applied on the first two jets (ordered with decreasing p_T), these selection removes $\sim 50\%$ of the $W(e\nu)+\text{jets}$ events.

► **TIV (TRACK ISOLATION VETO)** is defined as

$$TIV = \frac{1}{p_T(tk1)} \sum_{R \in \Delta R} (p_T)^j \quad (6.5)$$

A hollow cone $0.02 < \Delta < 0.3$ is drawn around each track with $p_T > 10$ GeV and $p_T > 15$ GeV at 10 TeV and 14 TeV cases respectively. The sum of the transverse momenta $(p_T)^j$ of the tracks inside the cone is then calculated for tracks with $(p_T)^j > 1$ GeV. Here $p_T(tk1)$ in the definition is the transverse momentum of the track of the cone excluded with the lower bound in order to avoid double counting. A small value of TIV is typical for well-isolated leptons and can be used to clean the samples by rejecting the events with tracks fulfilling $TIV < 0.1$ selection. Thus, the procedure results with the reduction of the number of events on $W(\mu\nu) + \text{jets}$ and top pair samples by a factor of 5 and 9, given 10 TeV and 14 TeV cases respectively.

Moreover, in order to suppress cosmic background, at least one vertex coming from the interaction point and at least two tracks with $p_T > 5\text{GeV}$ inside the leading jet cone is required.

6.6.3 III. Kinematic Cuts and QCD Reduction

In order to improve the background rejection, the most energetic jet in the event (leading jet, jet 1) is required to have $p_T(\text{jet } 1) > 200$ GeV and $|\eta(\text{jet } 1)| < 1.7 p_T(\text{jet } 1)$ at 14 TeV and $p_T(\text{jet } 1) > 350$ GeV and $|\eta(\text{jet } 1)| < 1.7 p_T(\text{jet } 1)$ at 10 TeV. After these selections, the signal

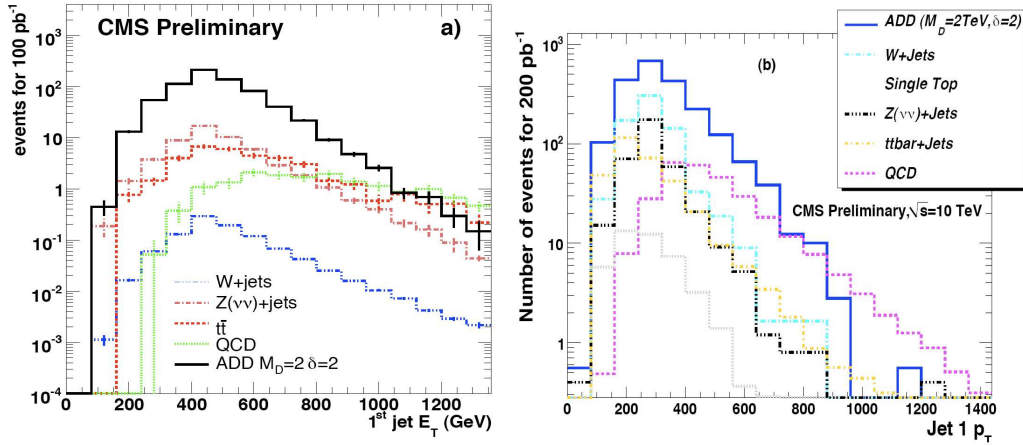


Figure 6.11: E_T and p_T distribution of the leading jet of ADD signal ($M_D = 2 \text{ TeV}$, $\delta = 2$) and relevant backgrounds. Event number is normalized to 100 pb^{-1} and to 200 pb^{-1} respectively.

jet multiplicity in figure 6.11 is peaked around 2 and rapidly decreases for higher number of jets.

As a result, events with more than two jets are vetoed. Since most of the dominant SM processes have the same p_T shape as the signal, the reductions of signal acceptances are comparable. The selection at this stage does not allow to enhance the signal/background ratio, but it is meant to define a kinematic region where subsequent cuts can be applied.

6.6.4 IV. Imposed Topological Constraints

In order to reduce the background further, it is worth to profit from the back-to-back topology of the signal selecting the events with an angular difference in the transverse plane $\phi(\text{jet } 1, ME_T) > 2.8$ and $\phi(\text{jet } 1, MH_T) > 2.8$. Then a fraction of the processes where missing energy does not recoil the jets will be rejected as illustrated in figure 6.12.

The complete set of selections are summarized in tables 6.9 and 6.10 for 14 TeV case and in tables 6.11 and 6.12 for 10 TeV case. After all the cuts reported on these tables are applied sequentially, the ME_T and MH_T distributions for signal and backgrounds are given in figure 6.13.

Remaining SM events contributing to the selected data samples are $Z(\rightarrow \nu\nu) + jets$ events. The amount of this background is estimated from the data using $W(\mu\nu) + jets$ events, called the *Control Sample*, the details are given in [47],[48].

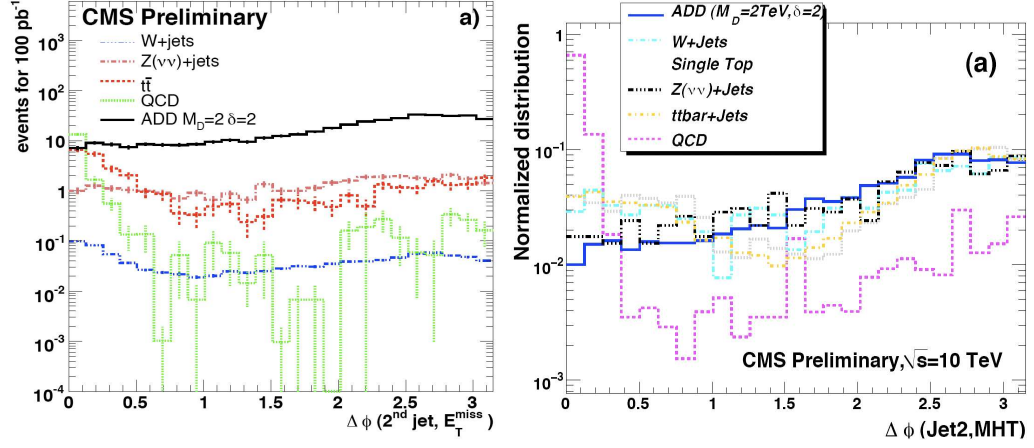


Figure 6.12: a) Angle in the transverse plane between the ME_T and the secondary jet. Selecting the events with $\phi(\text{jet } 2, ME_T) > 0.5$ may exclude a large part of the QCD together with the $t\bar{t}$ and W + Jets Backgrounds. b) The rejection is largely enhanced by requiring $\phi(\text{jet } 2, MHT) > 0.5$ at 10 TeV case in which a further reduction would be obtained by considering the multijet contribution of two orders of magnitude.

Table 6.9: Selected events of each group of cuts for the background samples of 14 TeV case normalized to 100 pb^{-1}

	$t\bar{t}$	Z($\nu\nu$)+Jets	QCD	W($e\nu$) +Jets	W($\mu\nu$) +Jets	W($\tau\nu$) +Jets
Trigger	3860	1280	4.92×10^5	1199	1617	1488
MET > 400 GeV	36.6	54.8	17.9	19.5	63.7	36.3
JEMF < 0.9	32.0	52.4	17.2	8.8	60.6	32.0
TIV < 0.1	12.2	46.3	14.2	4.3	5.9	13.0
$p_T(\text{jet } 1) > 350 \text{ GeV}$ $ \eta(\text{jet } 1) < 1.7$	9.8	36.6	11.8	3.3	4.5	9.9
numb jets < 3	2.2	28.9	4.6	2.3	2.8	6.9
$\Delta\phi > (\text{jet } 1, ME_T) > 2.8$	0.5	25.7	0.6	2.0	2.0	5.5
$\Delta\phi > (\text{jet } 1, ME_T) > 0.5$						

Table 6.10: Number of selected events for each group of cuts in four 14 TeV signal subsamples, normalized to 100 pb^{-1} . Uncertainties on efficiencies are only statistical.

	$\delta = 2$		$\delta = 4$	
	$M_D = 2 \text{ TeV}$	$M_D = 6 \text{ TeV}$	$M_D = 2 \text{ TeV}$	$M_D = 6 \text{ TeV}$
Trigger	3060	54.4	1190	7.98
MET > 400 GeV	691	12.1	244.7	3.05
JEMF < 0.9	658.6	11.6	231.8	2.9
TIV < 0.1	539.2	9.5	185.2	2.2
$p_T(\text{jet } 1) > 350 \text{ GeV}$ $ \eta(\text{jet } 1) < 1.7$	343.1	6.5	117.1	1.6
numb. jets < 3	286.8	5.4	98.3	1.2
$\Delta\phi > (\text{jet } 1, ME_T) > 2.8$	261.5	4.9	90.1	1.1
$\Delta\phi > (\text{jet } 1, ME_T) > 0.5$				
Total Efficiency %	8.1 ± 0.5	8.5 ± 3.8	7.1 ± 0.7	13.2 ± 13.2

Table 6.11: Number of selected events for each group of cuts in the 10 TeV background samples normalized to 200 pb^{-1}

	$t\bar{t}$	Z($\nu\nu$)+Jets	QCD	W($e\nu$) +Jets	W($\mu\nu$) +Jets	W($\tau\nu$) +Jets	single-t
Trigger	28,970	11,390	143.10 ⁶	31,320	19,320	20,600	4460
MHT > 250 GeV	318	358	288	90	391	230	44
JEMF < 0.9	52.5	305	214	31.9	38.5	90.9	7.2
TIV < 0.1							
p_T (jet 1) > 200 GeV $ \eta(\text{jet1}) < 1.7$	37.4	245	187	24.6	24.6	72.1	4.5
numb jets < 3	8.2	205.6	70.9	18.8	22.9	59.8	2.8
$\Delta\phi > (\text{jet1}, M_{E_T}) > 2.8$	6.4	182.5	0.2	17.2	19.7	46.7	2.3
$\Delta\phi > (\text{jet1}, M_{E_T}) > 0.5$							

Table 6.12: Number of selected events for each group of cuts in four 10 TeV signal subsamples, normalized to 200 pb^{-1} . The final efficiencies are quoted with only statistical uncertainties

	$(\delta = 2)$			$(\delta = 4)$	
	$M_D = 1 \text{ TeV}$	$M_D = 2 \text{ TeV}$	$M_D = 3 \text{ TeV}$	$M_D = 2 \text{ TeV}$	$M_D = 3 \text{ TeV}$
Trigger	51,000	6180	1370	2010	301
MHT > 250 GeV	11,140	2123	498	753	133
JEMF < 0.9	9572	1825	426	641	113
TIV < 0.1					
p_T (jet 1) > 200 GeV $ \eta(\text{jet1}) < 1.7$	6785	1368	314	487	88.4
numb jets < 3	5605	1044	401	374	64.4
$\Delta\phi > (\text{jet1}, M_{E_T}) > 2.8$	4934	906	206	322	55.8
$\Delta\phi > (\text{jet1}, M_{E_T}) > 0.5$					
Total Efficiency %	8.8±0.1	13.7±0.4	14.1±0.4	13.2±0.4	17.7±0.4

A simulation of a very clean, simple, monojet event simulated for the CMS Detector is given in the figure 6.14 where Red Cells: ECAL, Blue Cells: HCAL, Yellow Cones: JETS, Green Tracks: Tracks, Cyan Tracks: Electrons, Red Tracks: Muons, Red vector: MET and the purple line represents the Graviton give rise to the relevant signature.

6.7 Results and Systematics

Systematical uncertainties in the simulation of events at LHC are often significant contributions to the overall uncertainty in measurement, and in many cases, being comparable to the statistical uncertainties.

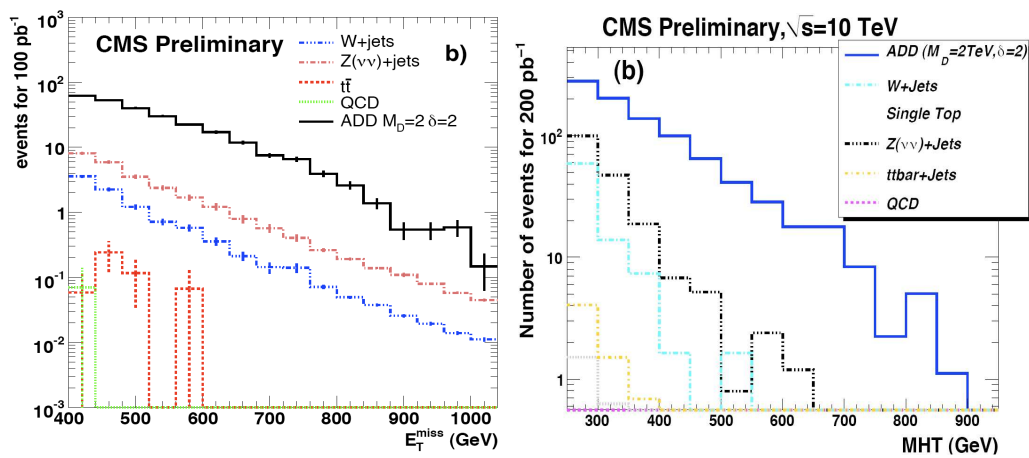


Figure 6.13: ME_T and MH_T distributions after all selections applied for $\sqrt{s}=14$ TeV and $\sqrt{s}=10$ TeV respectively

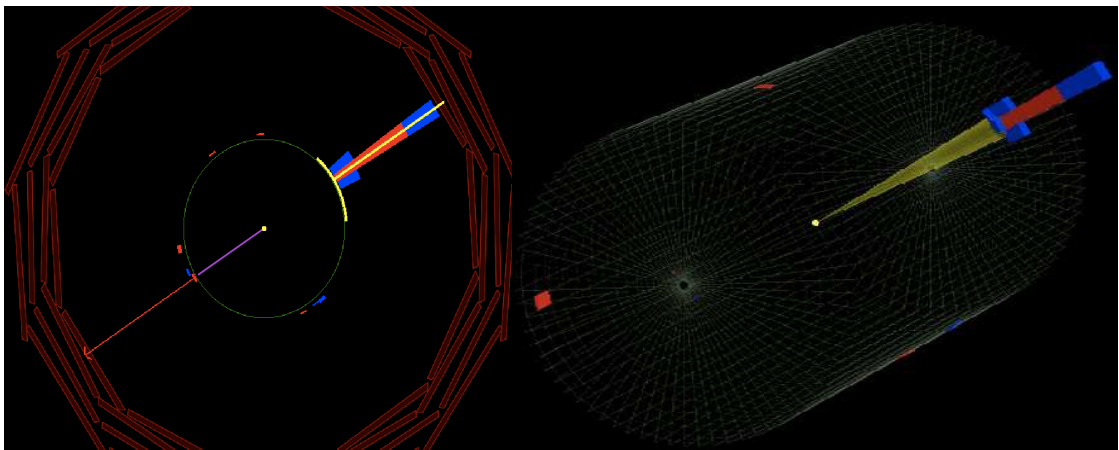


Figure 6.14: On the right, 3 Dimensional view of a very clean monojet event simulated for the CMS Detector is seen. On the left the projection of this event on the transverse plane is given.

6.7.1 Theoretical Uncertainties

The simulation in physics processes are performed with matrix element (ME) calculations at a certain order with corresponding coupling constants and it continues on with the parton showering (PS). PS process ends up with the construction of partons until a cutoff scale, where the perturbative evolution stops and fragmentation takes place.

On the other hand, an interesting event is accompanied by Underlying Event (UE) which encounters the relevant activity of pp interaction. The processes take place in the same bunch crossing with the minimum bias (MB) and Initial State Radiation (ISR) therefore each of these effects are required to be modelled and corresponding uncertainties have to be evaluated.

The systematical sources used to estimate the errors coming from above factors can result from QCD Radiation, PDF's, Fragmentation, UE and MB contributions.

► SYSTEMATICAL EFFECTS COMING FROM HARD PROCESSES OF ADD SIGNAL

The generation of hard gluon emission is made by using a higher leading order (LO) α_s generator tool SHERPA so the missing higher orders can be considered as a delicate source of uncertainty. Since jets can arise from higher order ME calculations during the shower evolution, the hard process under study drives the definition of Q^2 scale which directly enters the parametrization of PDF's and α_s hence in expression of the cross sections.

Estimation of cross section sensitivity to the theoretical errors is made by $Q = \sqrt{s}$ and the renormalization and factorization scale are varied from $Q/2$ to $2Q$ in the SHERPA generation step for different PDF choices. Results of the ADD signal benchmark point $M_D = 2, \delta = 2$ indicate (+11 % , -13 %) and (+7.5 % , -6.7 %) uncertainties for 14 TeV and 10 TeV cases respectively.

► PDF'S DESCRIPTION

The parton distribution functions of interacting particles describe the the probability density of partons and undergone hard scattering at the hard process scale Q^2 taking certain fraction. In order to evaluate theoretical uncertainties due to certain proton PDF's reweighting technique and Master Equation on the CTEQ61M model set is used and the cross section variation for the ADD signal with $M_D = 2$ and $\delta = 2$ is found as (+8.7 % , -6.7 %) for 14 TeV and (+11.5 % , -9.5 %) for 10 TeV analysis.

6.7.2 Experimental Uncertainties

► UNCERTAINTIES ON JET MEASUREMENTS

The response of an individual tile or crystal is known to limit accuracy from source calibration in the HCAL and ECAL, so an overall uncertainty of $\sim 15\%$ is expected for the jet energy scale.

The systematical effects taken into account for the mismeasurement of jets stem from jet energy resolution, jet direction uncertainties and the jet energy scale.

Systematics on the third jet veto and the other selection criterias have limited uncertainty on the jet resolution and transverse momenta of all jets were smeared by a Gaussian function accounting to 10% resolution. In order to handle direction uncertainties, transverse angle ϕ of all jets are also smeared by Gaussian centered on zero corresponding 0.1 radial resolution. The jet energy scale is emulated by shifting the jet 4 vector with a common $(1\pm\alpha)$ factor while α is assumed 10% irrespective to the jet energy. The summary of systematical effects can be found in table 6.13. The precision of the luminosity measurement in CMS taken as 10% for 100 pb^{-1} and 200 pb^{-1} integrated luminosities respectively.

Table 6.13: Overview of the Systematical Uncertainties given for 14 TeV and 10 TeV CM cases

Source	Signal events at $\sqrt{s} = 10\text{ TeV}$ (%)	Signal events at $\sqrt{s} = 14\text{TeV}$ (%)
Hard Process Scale	(+7.5, -6.7)	(+11, -13)
PDF	(+11.5, -9.5)	(+8.7, -6.7)
$p_T(\text{jet})$ and $\phi(\text{jet})$ Uncertainty	3	3
Jet Energy Scale Uncertainty	(+17.5, -15.9)	(+13.1, -16.2)

6.8 Discovery Potential and Exclusion Limits

Considering all the background sources and efficiency of ADD signal together with the systematical uncertainties discussed in the previous section, an estimation can be done to specify the discovery reach of the monojet signature for a likelihood function based on a hybrid bayesian approach.

After applying the optimal set of selections discussed before, the total number of background events denoted by N_B is estimated in order to modify the null hypothesis being the SM is true. The total number of cumulative background is given in the table 6.14

Table 6.14: Survived Background Events after combining all results

Backg. Events	Statistical Errors	Systematical Errors	Int.Lum (pb^{-1})
$N_B (\sqrt{s}=14 \text{ TeV})$			
30.7	± 6.8	(+2.7,-1.5)	100
$N_B (\sqrt{s}=10 \text{ TeV})$			
243	± 23	± 13	200

The significance estimator S_{PL} (Profile Likelihood) [65] is chosen to specify the discovery limit in order to incorporate systematical uncertainties into hypothesis tests. The significance estimator can be computed from a likelihood ratio, where the likelihood function is a Poisson distribution for the total number of observed events ($N_S + N_B$), multiplied by a Gaussian with N_B as mean and the total background error Δ_B as sigma. The analytic expression of the estimator can also be written with the parameters defined in table 6.15

$$S_{PL} = \sqrt{2} \left(n_{on} \ln \frac{n_{on}(1+\tau)}{n_{on} + n_{off}} + n_{off} \ln \frac{n_{off}(1+\tau)}{\tau(n_{on} + n_{off})} \right)^{1/2} \quad (6.6)$$

Symbol	definition
n_{off}	total observed in “off” (background) region
n_{on}	total observed in “on” (signal) region
n_{tot}	$n_{on} + n_{off}$
μ_s	true signal mean in “on” (signal) region
μ_b	true background mean in “on” (signal) region
$\hat{\mu}_b$	estimate of background mean in “on” (signal) region
σ_b	uncertainty on estimate $\hat{\mu}_b$ in “on” region
s	estimate of signal events in the “on” region = $n_{on} - \hat{\mu}_b$
f	relative uncertainty on $\hat{\mu}_b$; σ_b/μ_b
μ_{on}	true total mean in signal region = $\mu_s + \mu_b$
μ_{off}	true background mean in “off” (background) region
μ_{tot}	true total mean in “on” plus “off” regions = $\mu_{on} + \mu_{off}$
τ	ratio of background means in “off” and “on” regions: μ_{off}/μ_b
λ	ratio of Poisson means μ_{off}/μ_{on}
ρ	binomial parameter μ_{on}/μ_{tot}

Figure 6.15: Definitions of parameters for the S_{PL} Significance Estimator

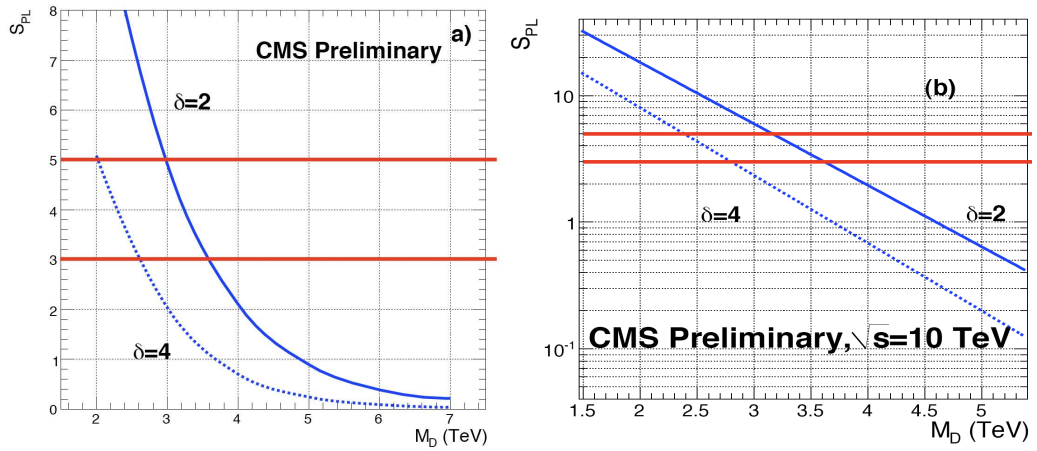


Figure 6.16: Discovery potential of the Monojet Signature as a function of M_D and δ for $\sqrt{s}=14$ TeV and $\sqrt{s}=10$ TeV respectively. The horizontal thick lines correspond to 3σ and 5σ significance levels.

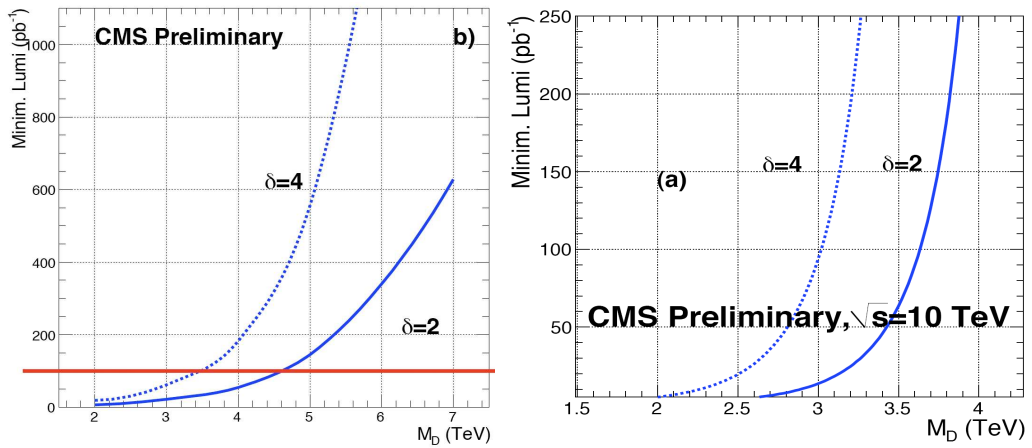


Figure 6.17: The fundamental scale M_D is correlated with the minimum integrated luminosity of $100 pb^{-1}$ and $200 pb^{-1}$ respectively at the %95 confidence level determining the exclusion limit of the monojet channel.

Correlating S_{PL} with the results of the parameter space (M_D, δ) of ADD Model, a discovery sensitivity plot for the monojet signature is derived as a function M_D and it is extrapolated on 100 pb^{-1} and 200 pb^{-1} integrated luminosities respectively given on figure 6.16

The alternative hypothesis to be rejected in favor of the null hypothesis can also be specified by the The 95% Confidence Level (CL), which scans the parameter space to minimize the negative Log Likelihood. This scanning operation is repeated for different benchmark points of the ADD Model and for the minimum integrated luminosity, it is extrapolated on the estimation of points marking the exclusion limit.

CHAPTER 7

CONCLUSIONS

A simulation study of the ADD model in the G+Jet channel corresponding ME_T + Monojet signature has been performed with the CMS detector. Using Monte Carlo generated events, two LHC scenarios, which are: a center-of-mass energy of 14 TeV with an integrated luminosity of 100 pb^{-1} , and a center-of-mass energy of 10 TeV with an integrated luminosity of 200 pb^{-1} are considered using offline selection techniques. The cut based analysis, which consists of jet selection, event topology and lepton veto are applied to optimize the significance of the set of selections and the excess over background is used to estimate the discovery potential of the regarded channel.

The significance estimator S_{PL} is correlated with the (M_D, δ) parameter set for 3 and 5 standard deviation criterions. As a result, 5σ discovery limits have been shown to indicate the values of the fundamental scale M_D lower than 3.69(2.72) TeV for $\delta = 2(4)$ at $\sqrt{s} = 14\text{TeV}$ center-of-mass energy. These limits are shown to be reduced $\sim 11\%$ for 10 TeV case as M_D is lower than 3.2(2.3) for $\delta = 2(4)$.

At %95 C.L., exclusion limits are estimated as $M_D = 4.61$ (3.46) TeV with $\delta = 2(4)$ for $\sqrt{s} = 14$ TeV case. These limits are also reduced $\sim 35\%$ for $\sqrt{s} = 10$ TeV case such that $M_D = 3(2)$ TeV for $\delta = 2(4)$. Thus, It is shown that the current Tevatron limits of the ADD model can be improved with a factor of 3 with the early LHC data in CMS detector using these selection techniques.

REFERENCES

- [1] L.M. Ricciardi and H.Umezawa, *Kibernetik* 4, 44 (1967)
- [2] Erik P. Verlinde, *On the Origin of Gravity and the Laws of Newton*, arXiv:1001.0785v1 [hep-th]
- [3] Hermann Weyl, *Gravitation and Electricity*, Sitzungsber. Preuss. Akad. Berlin (1918) 465
- [4] G. Nordstrom, *Phys. Zeit.* 15, 504 (1914).
- [5] Einstein, Albert, *Die Feldgleichungen der Gravitation (The Field Equations of Gravitation)* , Koniglich Preussische Akademie der Wissenschaften 844-847 (1915).
- [6] Ian Aitchison, *Supersymmetry in Particle Physics: An Elementary Introduction*, 1st Edition, Cambridge University Press (2007), 77-87
- [7] Joseph D.Lykken, 1996, Weak Scale Superstrings, *Phys. Rev.D*54 3693-3697 (Preprint hep-th/9603133)
- [8] Randall, Lisa; Sundrum, Raman (1999). *Large Mass Hierarchy from a Small Extra Dimension*. *Physical Review Letters* 83 (17): 3370–3373. doi:10.1103/PhysRevLett.83.3370.
- [9] Thomas G. Rizzo, *Identification of the Origin of Monojet Signatures at the LHC*. 10.1016/j.physletb.2008.06.043
- [10] V. H. Satheesh Kumar and P. K. Suresh, arXiv:hep-th/0606194.
- [11] CMS AN-2009/110, *Search for Large Extra Dimension in the ADD model using photon plus MET final state in early CMS data*

- [12] Bruce Knuteson *Solution to the LHC Inverse Problem*, arXiv:hep-ph/0608025v1
- [13] Nima Arkani Hamed, Philip Schuster, Natalia Toro, MARMOSSET: *emph*The Path from LHC Data to the New Standard Model via On-Shell Effective Theories, arXiv:hep-ph/0703088
- [14] Th. Kaluza, Sitz. Preuss. Akad. Wiss. Phys. Math. Kl 996 (1921)
- [15] Klein, Z. F. Physik 37 895 (1926)
- [16] G. Gabadadze, *ICTP Lectures on Large Extra Dimensions*, arXiv:hep-ph/0308112.
- [17] K.Akama, Lect. Notes Phys. 176, 267 (1982), *An Early Proposal of Brane World*
- [18] V. A. Rubakov and M. E. Shaposhnikov, *Do We live inside a Domain Wall* Phys. Lett. B 125 (1983) 136.
- [19] V.A.Rubakov, *Large and Infinite Extra Dimensions*, arXiv:hep-ph/0104152v2
- [20] N. Arkani-Hamed, S. Dimopoulos and G. R. Dvali, Phys. Lett. B **429**, 263 (1998) [arXiv:hep-ph/9803315].
- [21] I. Antoniadis, N. Arkani-Hamed, S. Dimopoulos and G. R. Dvali, Phys. Lett. B **436**, 257 (1998) [arXiv:hep-ph/9804398].
- [22] Joseph Lykken, Erich Poppitz and Sandip P. Trivedi, *Branes with GUTs and supersymmetry breaking*, hep-th/9806080 (June 1998)
- [23] M. Shifman, *LARGE EXTRA DIMENSIONS: Becoming acquainted with an alternative paradigm*, arXiv:hep-ph/0907.3074
- [24] G. F. Giudice, R. Rattazzi, J. D. Wells, Nucl. Phys. B544, 3 , *Quantum gravity and extra dimensions at high-energy colliders*
- [25] <http://lhc.web.cern.ch/lhc/...> last visited date:03/06/2010

- [26] Filip Moortgat, *A Document Preparation System Discovery potential of MSSM Higgs bosons using supersymmetric decay modes with the CMS Detector* Wetenschappen aan de Universiteit, Antwerpen, Doc.Thesis, 2004
- [27] Ikeda, H. et al., *Vertical Beam Size Measurement by Streak Camera Under Colliding and Single Beam Conditions in KEKB* Particle Accelerator Conference, 2005. PAC 2005.
- [28] *The CMS Collaboration The CMS experiment at the CERN LHC*, 2008 (JINST).
- [29] M.Weber, *The CMS Tracker* CERN, Geneva, Switzerland, CMS Collaboration, 2004.
- [30] CMS Collaboration, *The Tracker Project Technical Design Report*, CERN/LHCC **98-006** (1998) and CMS TDR 5, Addendum CERN/LHCC **20/016**
- [31] CMS Collaboration, *ECAL Technical Design Report*, CERN/LHCC **97-033** (1997)
- [32] CMS Collaboration, *Level-1 Trigger Technical Design Report*, CERN/LHCC **2000-038** (2000)
- [33] CMS Collaboration, *DAQ and High Level Trigger Technical Design Report*, CERN/LHCC **2002-026** (2002)
- [34] The CMS Collaboration and D.Acosta. *CMS Physics, Technical Design Report volume I : Detector Performance and Software*. CERN/LHC 2008-001, 2008.
- [35] CMS Collaboration, *ME_T performance in CMS*, PAS JME-07-001 (2007).
- [36] PAT:the CMS Physics Analysis Toolkit, CERN-CMS CR-2009/083
- [37] <https://twiki.cern.ch/twiki/bin/view/CMS/WorkBook> ...last visited date:21/04/2009
- [38] *Physics Analysis Tools for the CMS experiment at LHC*, CMS NOTE-2008/015

- [39] <https://twiki.cern.ch/twiki/bin/view/CMS/WorkBookPATWorkflow> ...last visited date:16/04/2010
- [40] G. F. Giudice, R. Rattazzi, J. D. Wells, Nucl. Phys. B544, 3 , *Quantum gravity and extra dimensions at high-energy colliders*
- [41] CDF Collaboration, Phys. Rev. Lett. 101, 181602 (2008)
- [42] DELPHI Collaboration, Eur. Phys. J. C 38, 395 (2005) ; L3 Collaboration, Phys. Lett. B 587, 16 (2004)
- [43] $D\phi$ Collaboration, Phys. Rev. Lett. 101, 011601 (2008)
- [44] $D\phi$ Collaboration, Phys. Rev. Lett. 90, 251802 (2003)
- [45] V. Krutelyov, 0807.0645v1[hep-ex]
- [46] L. Vacavant, Eur. Phys. J. C33, S924 (2004)
- [47] L. Benucci, M. Cardaci, A. De Roeck, U. Emrah Surat, L. Sala, P. Van Mechelen CERN-CMS-AN-2008/073
- [48] L. Benucci, M. Cardaci, A. De Roeck, U. Emrah Surat, L. Sala, L. Vergili CERN-CMS-AN-2009/109
- [49] C. D. Hoyle et al., Phys. Rev. Lett 86, 1418
- [50] V. H. Satheeshkumar and P. K. Suresh, 0805.3429v1[astro-ph]
- [51] Matteo Cacciari, et.al. Pile Up subtraction using jet areas, Physcis Letters B. 659 (2008) 119-126
- [52] B. Abbott et al. ($D\phi$ Collaboration), Phys. Rev. Lett. 86, 1707 (2001); L.Babukhadia, Ph.D, Dissertation, University of Arizona, Tucson, Arizona, USA 1999,
- [53] V.Gaultney, et.al. CMSAN-2009/052, Beam Halo Tagging Study Using Correlations in the Electromagnetic and Hadronic Calorimeters

- [54] T. Gleisberg, S. Hoeche, F. Krauss et al. JHEP 0402, 056 (2004), <http://www.sherpa-mc.de> ...last visited date:21/04/2009
- [55] For details, see <https://twiki.cern.ch/twiki/bin/view/CMS/ProductionSummer2008>...last visited date:12/04/2008
- [56] J. Alwall et al., MadGraph/MadEvent v4: The New Web Generation, JHEP 0709 (2007) 028, arXiv:hep-ph/0706.2334.
- [57] S. Houche et al., hep-ph/0602031
- [58] For details, see <https://twiki.cern.ch/twiki/bin/view/CMS/CSA07>...last visited date:03/08/2008
- [59] For details, see <https://twiki.cern.ch/twiki/bin/view/CMS/SWGuidePAT>...last visited date:03/06/2010
- [60] CMS Collaboration, CMS-PAS-JME-07-003
- [61] CMS Collaboration, CMS-PAS-JME-08-002
- [62] For details, see <http://indico.cern.ch/conferenceDisplay.py?confId=33540> and <http://indico.cern.ch/conferenceDisplay.py?confId=32795>...last visited date:24/09/2008
- [63] For details, see <https://twiki.cern.ch/twiki/bin/view/CMS/TSG03091E31> ...last visited date:06/01/2009
- [64] M. Spiropulu, PhD Thesis, UMI-99-88600
- [65] R. D. Cousins, J. T. Linnemann, and J. Tucker, ‘ Evaluation of three methods for calculating statistical significance when incorporating a systematic uncertainty into a test of the background-only hypothesis for a Poisson process’, NIM A595 (2008) 480, arXiv:physics/0702156v3.
- [66] Liu, H., Mashhoon, B. (2000). Phys. Lett. A 272, 26, gr-qc/0005079

APPENDIX A

ADAPTED TRIGGERS FOR 10 TeV SEARCH

Table A.1: Efficiency of the triggers before the selections are applied together with the number of events survived

8E29 MENUS							
Path	$M_D = 1, \delta = 6$	$M_D = 2, \delta = 2$	$M_D = 2, \delta = 4$	$M_D = 2, \delta = 6$	$M_D = 3, \delta = 2$	$M_D = 3, \delta = 4$	$M_D = 3, \delta = 6$
L1_ETM30	8782.4 (98.8%)	6576.1 (99.5%)	2114.5 (99.4%)	910.8 (99.4%)	1447.8 (99.4%)	313.0 (99.4%)	114.9 (99.5%)
HLT_MET35	8766.1 (99.8%)	6566.7 (99.9%)	2110.5 (99.8%)	909.3 (99.8%)	1446.3 (99.9%)	312.6 (99.9%)	114.7 (99.8%)
1E31 MENUS							
L1_ETM40	8679.4 (97.6%)	6531.0 (98.9%)	2101.2 (98.7%)	902.7 (98.5%)	1437.8 (98.7%)	311.3 (98.9%)	114.1 (98.8%)
HLT_MET50	8638.6 (99.5%)	6513.2 (99.7%)	2092.6 (99.6%)	897.8 (99.5%)	1433.6 (99.7%)	310.3 (99.7%)	113.7 (99.7%)
L1_ETT60	8872.7 (99.8%)	6601.8 (99.9%)	2126.5 (99.9%)	915.1 (99.9%)	1454.3 (99.9%)	314.3 (99.8%)	115.4 (99.9%)
HLT_SumET120	8549.7 (96.4%)	6456.3 (97.8%)	2088.3 (98.2%)	897.3 (98.1%)	1425.4 (98.0%)	309.8 (98.6%)	113.7 (98.5%)
L1_SingleJet70	8815.7 (99.1%)	6566.7 (99.4%)	2120.5 (99.7%)	912.9 (99.7%)	1447.7 (99.4%)	313.8 (99.7%)	115.3 (99.8%)
HLT_Jet110	8160.0 (92.6%)	6199.9 (94.4%)	2023.9 (95.4%)	874.4 (95.8%)	1367.4 (94.5%)	301.9 (96.2%)	111.6 (96.8%)
L1 Online HLT Offline							
L1_HTT200	6862.6 (77.2%)	5570.7 (84.3%)	1852.6 (87.1%)	793.7 (86.6%)	1241.8 (85.3%)	279.5 (88.8%)	102.6 (88.9%)
HLT_HT300	2817.8 (41.1%)	3139.6 (56.4%)	1096.7 (59.2%)	465.6 (58.7%)	725.6 (58.4%)	177.8 (63.6%)	65.6 (64.0%)
13_HLT_MHT100	2588.8 (91.9%)	3022.5 (96.3%)	1052.8 (96.0%)	441.5 (94.8%)	701.6 (96.7%)	171.3 (96.3%)	62.8 (95.7%)
L1 Offline HLT Offline							
L1_HT200	7613.1 (85.6%)	5910.7 (89.5%)	1947.7 (91.5%)	838.1 (91.5%)	1317.7 (90.5%)	291.1 (92.5%)	107.4 (93.1%)
HLT_HT300	2817.8 (37.0%)	3140.1 (53.1%)	1096.7 (56.3%)	465.6 (55.6%)	725.6 (55.1%)	177.8 (61.1%)	65.6 (61.1%)
HLT_MHT100	2588.8 (91.9%)	3023.1 (96.3%)	1052.8 (96.0%)	441.5 (94.8%)	701.6 (96.7%)	171.3 (96.3%)	62.8 (95.7%)

Table A.2: Efficiency of the triggers after the selections are applied together with the number of events survived

8E29 MENUS							
Path	$M_D = 1, \delta = 6$	$M_D = 2, \delta = 2$	$M_D = 2, \delta = 4$	$M_D = 2, \delta = 6$	$M_D = 3, \delta = 2$	$M_D = 3, \delta = 4$	$M_D = 3, \delta = 6$
L1_ETM30	1507.1 (100.0%)	1543.3 (100.0%)	532.2 (100.0%)	230.3 (100.0%)	339.7 (100.0%)	84.5 (100.0%)	32.6 (100.0%)
HLT_MET35	1507.1 (100.0%)	1543.3 (100.0%)	532.2 (100.0%)	230.3 (100.0%)	339.7 (100.0%)	84.5 (100.0%)	32.6 (100.0%)
1E31 MENUS							
L1_ETM40	1507.1 (100.0%)	1543.3 (100.0%)	532.2 (100.0%)	230.3 (100.0%)	339.7 (100.0%)	84.5 (100.0%)	32.6 (100.0%)
HLT_MET50	1507.1 (100.0%)	1543.3 (100.0%)	532.2 (100.0%)	230.3 (100.0%)	339.7 (100.0%)	84.5 (100.0%)	32.6 (100.0%)
L1_ETT60	1507.1 (100.0%)	1543.3 (100.0%)	532.2 (100.0%)	230.3 (100.0%)	339.7 (100.0%)	84.5 (100.0%)	32.6 (100.0%)
HLT_SumET120	1507.1 (100.0%)	1543.3 (100.0%)	532.2 (100.0%)	230.3 (100.0%)	339.7 (100.0%)	84.5 (100.0%)	32.6 (100.0%)
L1_SingleJet70	1507.1 (100.0%)	1543.3 (100.0%)	532.2 (100.0%)	230.3 (100.0%)	339.7 (100.0%)	84.5 (100.0%)	32.6 (100.0%)
HLT_Jet110	1507.1 (100.0%)	1543.3 (100.0%)	532.2 (100.0%)	230.3 (100.0%)	339.7 (100.0%)	84.5 (100.0%)	32.6 (100.0%)
L1 Online HLT Offline							
L1_HTT200	1463.4 (97.1%)	1516.5 (98.3%)	524.2 (98.5%)	226.7 (98.5%)	335.8 (98.9%)	83.5 (98.8%)	32.2 (98.9%)
HLT_HT300	522.4 (35.7%)	924.6 (61.0%)	324.2 (61.8%)	134.1 (59.2%)	204.7 (61.0%)	54.7 (65.5%)	20.7 (64.4%)
HLT_MHT100	522.4 (100.0%)	924.6 (100.0%)	324.2 (100.0%)	134.1 (100.0%)	204.7 (100.0%)	54.7 (100.0%)	20.7 (100.0%)
L1 Offline HLT Offline							
L1_HT_200	1507.1 (100.0%)	1543.3 (100.0%)	532.2 (100.0%)	230.3 (100.0%)	339.7 (100.0%)	84.5 (100.0%)	32.6 (100.0%)
HLT_HT300	522.4 (34.7%)	924.6 (59.9%)	324.2 (60.9%)	134.1 (58.2%)	204.7 (60.3%)	54.7 (64.7%)	20.7 (63.7%)
HLT_MHT100	522.4 (100.0%)	924.6 (100.0%)	324.2 (100.0%)	134.1 (100.0%)	204.7 (100.0%)	54.7 (100.0%)	20.7 (100.0%)